INVESTIGATION OF DYE SENSITIZED SOLAR CELLS FABRICATED BY SPRAY PYROLYSIS

by

MAHİR GÜLEN

THESIS SUBMITTED TO

THE GRADUATE SCHOOL OF NATURAL AND APPLIED SCIENCES

OF

THE ABANT İZZET BAYSAL UNIVERSITY

IN PARTIAL FULFILLMENT OF THE REQUIREMENTS FOR THE

DEGREE

OF

MASTER OF SCIENCE

IN

THE DEPARTMENT OF PHYSICS

JUNE 2012

Approval of the Graduate School of Natural and Applied Science

Prof. Dr. Nihat ÇELEBİ

Director

I certify that this thesis satisfies all the requirements as a thesis for the degree of Master of Science.

Assoc. Prof. Dr. Cabir TERZIOĞLU

Head of Physics Department

This is to certify that we have read this thesis and that in our opinion it is fully adequate, in scope and quality as a thesis for the degree of Master of Science.

Prof. Dr. Ahmet VARİLCİ

Supervisor

Examining Committee Members:

1. Prof. Dr. Ahmet VARİLCİ …….
2. Assoc. Prof. Dr. Osman GÖRÜR …….
3. Assist. Prof. Dr. Erhan BUDAK ……

ABSTRACT

INVESTIGATION OF DYE SENSITIZED SOLAR CELLS FABRICATED BY SPRAY PYROLYSIS

GÜLEN, Mahir

Master of Science, Department of Physics

Supervisor: Prof. Dr. Ahmet VARİLCİ

June 2012, 77 Pages

In this thesis, we investigated the efficiency and maximum power of the dye-sensitized solar cell (DSSC) produced with the aid of spray pyrolysis method in the voltage range of 0-0.7 V. The fabrication of the cell contains 3 parts. (I) Deposition of Indium Tin Oxide (ITO) thin film on soda lime glass was carried out by DC magnetron reactive sputtering technique at 100 watt using an ITO ceramic target (In_2O_3:SnO_2, 90:10 wt%) in argon atmosphere at room temperature. Then, the ITO film prepared was annealed at different temperature and time and the best annealing ambient was observed to be 400 °C for 2 h. The film produced was analyzed by means of X–ray diffractometer, ultraviolet visible

spectrometer and atomic force microscopy investigations. (II) Titanium dioxide film (TiO_2) was deposited on the ITO surface of glass soda lime by spray pyrolysis method after the best annealing environment was determined for the fabrication of the TiO_2 thin film. Scanning Electron Microscopy (SEM), X–ray diffractometer (XRD), atomic force microscopy (AFM) and ultra-violet spectrometer (Uv-Vis) measurements were performed for the TiO_2 film characterization. (III) Coating of the platinum (Pt) layer on ITO surface of soda lime glass was performed by DC magnetron reactive sputtering technique at 100 watt using a target composed of 90 wt% Pt in argon atmosphere at room temperature. This sandwich system was filled by electrolyte liquid called as iodide/tri-iodide (I^- / I_3^-) of which the platinum layer was used to be the catalyst for the regeneration. Additionally, current-voltage measurement of the DSSC prepared was conducted under an illumination of 1kW/m^2 and active area of 4cm^2. The efficiency and maximum power of the cell are determined from Fill Factor. The results show that the former was found to be about 5.05 % when the maximum power was observed to be about 20.1mW. According to the results obtained, the dye-sensitized solar cell might be used as alternative energy source.

Key words: Dye-Sensitized Solar Cell; Spray Pyrolysis; Efficiency; Maximum power; SEM; XRD; Uv-Vis; AFM.

ÖZET

SPREY METODU KULLANILARAK ÜRETİLEN BOYA İLE HASSASLAŞTIRILMIŞ GÜNEŞ PİLLERİNİN İNCELENMESİ

GÜLEN, Mahir

Yüksek Lisans, Fizik Bölümü

Tez Danışmanı: Prof. Dr. Ahmet VARİLCİ

Haziran 2011, 77 Sayfa

Bu tezde, sprey püskürtme metodu yardımı ile üretilen boyayla hassaslaştırılan güneş pilinin verimini ve maksimum gününü 0–0.7 Volt aralığında inceledik. Pilin üretimi 3 kısımdan oluşur. (I) DC manyetron duyarlı püskürtme tekniği ile 100 vatta ITO seramik (In_2O_3:SnO_2, 90:10 wt%) hedef kullanılarak soda camının üstüne indiyum kalay oksit (ITO) ince filmin kaplanması oda sıcaklığında, argon atmosferinde gerçekleştirildi. Sonra, hazırlanan ITO film farklı sıcaklık ve sürede tavlandı ve en iyi tavlama ortamının 400 °C de 2 saat olarak gözlemlendi. Üretilen film X-ray difraktometre, görünür bölge ve mor ötesi spektroskopisi ve atomik kuvvet mikroskobu incelemeleri vasıtasıyla analiz edildi. (II) TiO_2 film üretimi için en iyi tavlama ortamı belirlendikten sonra,

titanyum dioksit film soda camın ITO yüzeyi üzerine sprey püskürtme metodu kullanılarak kaplandı. TiO_2 film karakterizesi için Taramalı elektron mikroskobu (SEM), X–ray difraktometre (XRD), atomik kuvvet mikroskobu (AFM), görünür bölge ve mor ötesi spektroskopi (Uv-Vis) ölçümleri yapıldı. (III) Soda camının ITO yüzeyi üzerine Platin (Pt) tabaka kaplaması DC püskürtme tekniği ile 100 vatta % 90 Pt içeren hedef kullanılarak oda sıcaklığında, argon atmosferinde yapıldı. Bu sandviç sistem, iodide/tri-iodide (I^- / I_3^-) adı verilen sıvı elektrolit ile dolduruldu. Platin tabaka elektron rejenerasyonu için kataliz olarak kullanıldı. Ek olarak, hazırlanan DSSC pilinin akım-voltaj ölçümü 1kW/m^2 ışık altında ve 4cm^2 aktif alanda gerçekleştirildi. Verim ve maksimum güç doluluk faktöründen belirlendi. Sonuçlar gösteriyor ki verim % 5.05 civarında bulunurken maksimum güç 20.1mW olarak gözlemlendi. Elde edilen sonuçlara göre, boyayla hassaslaştırılmış güneş pili alternatif enerji kaynağı olarak kullanılabilir.

Anahtar Kelimeler: Boyayla Hassaslaştırılan Güneş Pili; Sprey Püskürtme; Verim; Maksimum Güç; SEM; XRD; Uv-Vis; AFM.

TO MY MOTHER…

ACKNOWLEDGEMENT

It is a great pleasure to thank many people who have contributed to the completion of this thesis.

First of all, I would like to thank my thesis supervisor, Prof. Dr. Ahmet Varilci for his guidance, support, encouragement and patience during the preparation of this thesis. He taught not only a great deal of major viewpoints about physics but also to be a decisive and patient researcher.

I also acknowledge to my supervisor Prof. Dr. Ahmet Varilci again, Assoc. Prof. Dr. Cabir Terzioğlu and Asist. Prof. Dr. Erhan Budak along with my advisor for serving on my thesis committee.

I am grateful to R. A. Gürcan Yıldırım for their effort, kind help and support during the preparation of sample and carrying out experimental measurements.

At last, I want to thank my family for their continuous support, patience and encouragement which made it possible for me to keep on my study.

TABLE OF CONTENTS

LIST OF TABLES

LIST OF FIGURES

CHAPTER 1

INTRODUCTION

1.1 Why Is The Solar Energy Important?

As the world of economy continues to grow and as industrialization of developing countries go on, the need for energy will increase. Economic growth is proportional with employable energy sources. Beginning with the surge in coal use which accompanied the Industrial Revolution, energy consumption has steadily transitioned from wood and biomass to fossil fuels. The primary development of solar technologies starting in the 1860s was driven by an expectation that coal would soon become scarce. However improvement of solar technologies stagnated in the early 20^{th} century in the face of the increment availability, economy, and utility of coal and petroleum [1]. The 1973 oil embargo and 1979 energy crisis caused a reorganization of energy policies around the world and brought renewed attention to improvement solar technologies [2,3]. Deployment strategies concentrated on incentive programs such as the Federal Photovoltaic Utilization Program in the US and the Sunshine Program in Japan. Other efforts involved the formation of research facilities in the US (SERI, now NREL), Japan (NEDO), and Germany (Fraunhofer Institute for Solar Energy Systems ISE).

The traditional obtaining of energy methods as coal, petroleum and gas are an important reason of pollution. Moreover, the International Energy Agency said that "the development of affordable, inexhaustible and clean solar energy technologies will have huge longer term benefits" in 2011. It will surge energy security of countries through reliance on an indigenous, inexhaustible and mostly import-independent reserve, increase sustainability, decrease pollution, lower the costs of mitigating climate change, and keep fossil fuel prices lower than otherwise. Moreover, the reality of the consuming of the fossil fuels is known and all of developed countries look for other ways of supplying energy in future. The general consideration that, the renewable energy source which is more sensitive to the environment should be used for energy needs. The solar energy and several types of other powers such as wind power, hydroelectric, nuclear power, modern biomass power, geothermal power etc. are seen to be major power in future. Due to the technological improvements and economic problems, deriving benefit from these alternative energy sources which are known new and renewable energy source did not come out adequate level. Besides, workings of Ar-Ge continue on technologies of the geothermal, photovoltaic and wind power on sea. Whereas the storage of thermal energy in underground is to become widespread especially in developed countries, in the technology of hydrogen energy is going on consistently. Among all the clean energy resources, solar power is the most powerful energy resource.

1.2 Historical Improvement of Solar Cell

After the photovoltaic effect was noted by Edmund Bequerel, in 1877 the photovoltaic effect was defined in more detail by William Adams and Richard Day. In 1876, William Adams and Richard Day found that a photocurrent could be fabricated in a sample of selenium when contacted by two heated platinum contacts. The photovoltaic action of the selenium varied from its photoconductive action in that a current was manufactured spontaneously by the action of light and no external power supply was needed. In this early the photovoltaic device, a recondition junction had been designed between the semiconductor and the metal contact. In 1894, Charles Fritts prepared what was probably the first huge area solar cell by compressing a layer of selenium between gold and another metal. In the following years photovoltaic effects were watched over in copper-copper oxide thin film constructions, in lead sulphide and thallium sulphide. These early cells were thin film Schottky barrier devices, where a semitransparent layer of metal invested on top of the semiconductor satisfied both the asymmetric electronic junction, which is required for photovoltaic action and access to the junction for the incoming light. The photovoltaic effect of constructions like this was relevant to the existence of a barrier to current flow at one of the semiconductor-metal interfaces (rectifying action) by Goldman and Brodsky in 1914. After that, during the 1930s, the theory of metal-semiconductor barrier layers was improved by Walter Schottky, Neville Mott and others.

However, it was not the photovoltaic features of materials like selenium which excited researchers, but it was the photoconductivity. The fact that the current created was proportional to the intensity of the incoming light and linked

to the wavelength in a definite way meant that photoconductive materials were ideal for photographic light meters. The photovoltaic effect where in barrier constructions was an inserted benefit, meaning that the light meter could operate without a power supply.

It was not till the 1950s, with the improvement of good quality silicon wafers for applications in the new solid state electronics, that potentially available quantities of power were fabricated by photovoltaic devices in crystalline silicon. In the 1950s, the improvement of silicon electronics followed the discovery of a way to manufacture p-n junctions in silicon. Naturally n type silicon wafers evolved a p type skin when exposed to the gas boron tri-chloride and part of the skin could be etched away to give access to the n type layer beneath. These p-n junction structures fabricated much better rectifying action than Schottky barriers, and better attitude of photovoltaic. The first silicon solar cell was reported by Chapin, Fuller and Pearson in 1954 and transformed sunlight with an efficiency of 6%, six times higher than the best previous attempt. That picture was to rise significantly over the following years and periods but, at an estimated production cost of some $200 per Watt, these cells were not seriously thought out for power production for several years. Nevertheless, the early silicon solar cell did introduce the possibility of power production in remote locations where fuel could not easily be delivered. The obvious application was to satellites where the required of reliability and low weight made the cost of the cells unimportant and during the 1950s and 60s, silicon solar cells were widely improved for applications in space.

Also in 1954, a cadmium sulphide p-n junction was fabricated with efficiency of 6%, and in the following years employments of p-n junction photovoltaic devices in gallium arsenide, indium phosphide and cadmium telluride were stimulated by theoretical work indicating that these materials would deal a higher efficiency. However, silicon remained and remains the primary photovoltaic material, profit from the advances of silicon technology for the microelectronics industry. Short histories of the solar cell are given elsewhere [4].

In the 1970s the crisis in energy source experienced by the oil-dependent western world led to a sudden growth of interest in alternative sources of energy, and financing for research and improvement in those areas. Photovoltaics were a subject of intense attention during this period, and a range of approaches for fabricating photovoltaic devices and materials more cheaply and for improving device efficiency were explored. Routes to lower cost involved photo electrochemical junctions, and alternate materials such as polycrystalline silicon, amorphous silicon, other thin films materials and organic conductors. Approaches for higher efficiency involved tandem and other multiple band gap designs. Although none of these led to widespread commercial improvement, our thoughtful of the science of photovoltaic is mainly rooted in this period.

During the 1990s, domain in photovoltaics expanded, during with growing realization of the need to secure sources of electricity alternative to fossil fuels. The trend coincides with the widespread liberalization of the electricity markets and growing recognition of the viability of decentralized power. Along this period, the economics of photovoltaics developed mainly through economies of scale. In the late 1990s the photovoltaic fabrication increased at a rate of 15-25%

per annum, driving a reduction in cost. Photovoltaics first became competitive in bunch where traditional electricity supply is most expensive, for example, for remote low power applications such as navigation, telecommunications, and rural electrification and for improvement of supply in grid-connected loads at peak use [5,6].As prices decline, new markets are opened up. An important illustration is building integrated photovoltaic applications, where the price of the photovoltaic system is offset by the savings in construction materials.

1.3 Solar Power

Solar power is the transformation of sunlight into electricity, either directly using photovoltaics (PV), or incidentally using concentrated solar power (CSP). For focusing a large area of sunlight into a small beam is used lenses or mirrors and tracking systems by CSP. PV is a mechanism that transforms light into electrical current using the photoelectric effect without any external energy source. The Sun is amazingly powerful in spite of it is150 million kilometers away from the earth. Moreover, just the tiny fraction of the Sun's energy that arrives at the Earth (around a hundredth of a millionth of a percent) is enough to meet all our power needs many times over. As a matter of fact, every minute, enough energy hits the Earth to meet our demands for a whole year, if only we could harness it appropriately. The Earth obtains 174 petawatts (PW) of incident solar radiation (insolation) at the upper atmosphere. Approximately 30% is reflected back to space while the rest is absorbed by clouds, oceans and land masses. The spectrum of solar light at the Earth's surface is mostly spread across the visible and near-infrared intervals with a small part in the near-ultraviolet. The total solar energy absorbed by Earth's atmosphere, oceans and land masses is

approximately 3,850,000exajoules (EJ) per year. In 2002, this was more energy in one hour than the world employed in one year. Photosynthesis captures nearly 3,000 EJ per year in biomass. The volume of solar energy reaching the surface of the planet is so massive that in one year it is about twice as much as will ever be enhanced from all of the Earth's non-renewable resources of coal, oil, natural gas, and mined uranium combine. Solar energy can be obtained in different levels around the world. Depending on a geographical position the closer to the equator the more "potential" solar energy is available. Solar energy, radiant light and heat from the sun, has been obtained by humans since ancient times using a range of ever-evolving technologies. Solar energy technologies involve solar heating, solar thermal electricity, solar architecture and solar photovoltaics. Solar technologies are broadly branded as either passive solar or active solar depending on the way they capture, transform and distribute solar energy. Passive solar techniques include orienting a building to the Sun, selecting materials with favorable thermal mass or light dispersing features, and designing spaces that naturally circulate air. Active solar techniques contain the use of photovoltaic panels and solar thermal collectors to harness the energy.

1.4 Photovoltaic Cells

A solar cell, or photovoltaic cell (PV), is a device that transforms light into electric current using the photoelectric effect. The photoelectric effect was first noted by a French physicist, Edmund Bequerel, in 1839, who found that certain materials would generate small amounts of electric current when exposed to light. Some materials expose a property known as the photoelectric effect that causes

them to absorb photons of light and release electrons. When these free electrons are captured, results of an electric current that can be used as electricity.

1.4.1 How Does The Photovoltaic Cell Work?

PV cells transform sunlight directly into electricity without creating any air or water pollution. As shown in figure 1.1, PV cells are made of at least two layers of semiconductor material. One layer has a positive charge, the other negative. When light enters the cell, some of the photons from the light are absorbed by the semiconductor atoms, freeing electrons from the cell's negative layer to flow through an external circuit and back into the positive layer. This flow of electrons produces electric current.

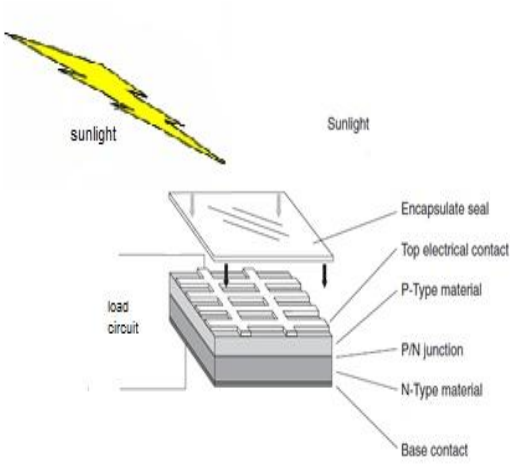

Figure 1. 1: Construction of basic solar cell

CHAPTER 2

SOLAR CELLS

2.1 Single Crystal and Poly Cristal Structure of Silicon Solar Cells

What is the difference between single crystalline and poly crystalline solar cells? The difference between single crystalline and polycrystalline cells is simply that one is fabricated from a single crystal of silicon and the other is fabricated from a piece of silicon including of several crystals. Since polycrystalline cells include many crystals, they have a less perfect surface than single crystalline cells. This means that they absorb slightly less solar energy and obtain slightly less electricity per square meter. On the other hand, the method of fabricating the silicon for a polycrystalline cell is much simpler, so these cells are commonly cheaper per square meter.

On balance, the cost of single crystalline and polycrystalline based panels per Watt of power output works out about the same, but the polycrystalline panels will be slightly greater than equivalent single crystalline panels. This is commonly not a problem unless you have a very limited area available for the installation, in which case you will want to maximize the power output per square meter.

Single crystalline and polycrystalline can also look different. Single crystalline cells will usually have a perfectly uniform appearance, but

polycrystalline cells will appear “grainy” think of how a granite worktop looks and you’ll get the idea. From a distance this will not be noticeable, so if they are going on your roof this is unlikely to worry you.

2.1.1 Operation of Crystalline Silicon Cells

The typical silicon solar cell is built on a semiconductor p-n junction. The cell contains of n-doped and p-doped semiconductor layers. When the two layers are located in contact with each other the p-n junction is formed by the charge transporters from n-type and p-type layers separately [7]. Figures 2.1 and 2.2 represent the effect of doping on the system. n-type semiconductors are obtained by doping such as arsenic or phosphorus atoms having an excess valence electron in contact with silicon. The n-type doping occurs in energy states just below the conduction band of the host semiconductor.

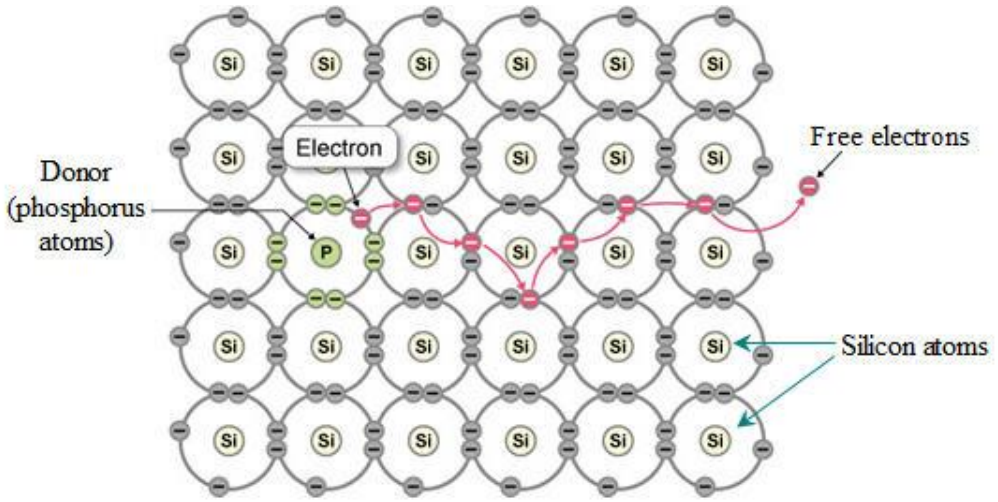

Figure 2. 1: n-type semiconductor

p-type semiconductors are generally carried out by adding impurity (doping). For example; the silicon with boron, aluminum or gallium atoms obtaining one valence electron less than the enveloping atoms can be used. p-type doping occurs in empty aspect with energy subtly above the valence band (VB) of the semiconductor.

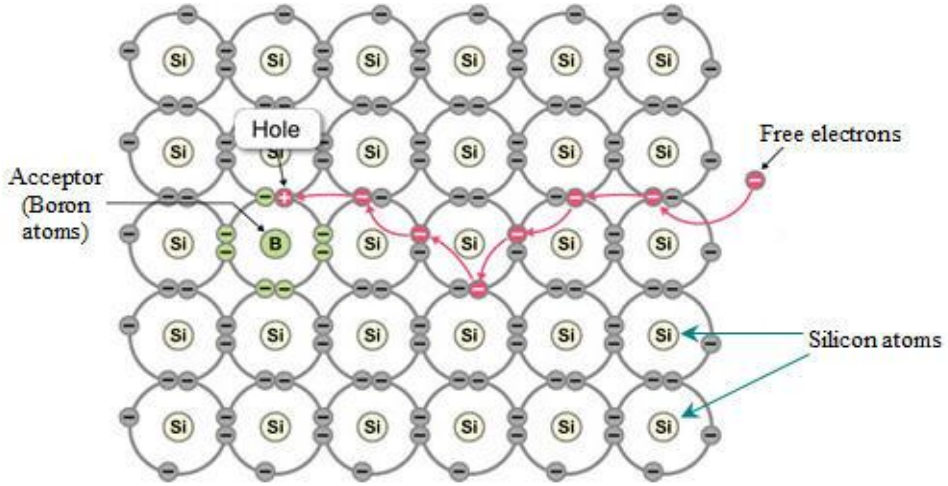

Figure 2. 2:p-type semiconductor

When the n-type and p-type semiconductors are combined together, a migration of electrons and holes across the junction happen until equilibrium is reached. This phenomenon is called as the equalization of the Fermi Energy level in the materials. This process constructs a depletion region (represented in fig. 2.3) near the junction where there are almost no free charges. A potential difference (electric field) stems from the depletion region.

Under illumination of the pn-junction, photons are absorbed by excitation of electrons from the valence band to the conduction band exit holes to the valence band. The electrons and holes are more or fewer free to migrate in the

semiconductor by drift due to potential gradients and by diffusion due to concentration gradients due to the high crystallinity of the semiconductor, which is vital for fine operation. The existence of the resident electric field in the pn junction zone is the source of photovoltaic activity in the cell. Under illumination, a large number of electrons and holes are created in the semiconductor material. Sectional charge carriers created in the depletion region of the pn-junction, or within their diffusion length from it, are removed to the opposite side of the junction by the resident electric field of the junction. Under illumination, electrons are hence accumulated in the n-type material and holes in the p-type material, producing voltage between the opposite sides of the pn-combination and electrical contacts attached to them, as well as current through an external load attached between the contacts [11].

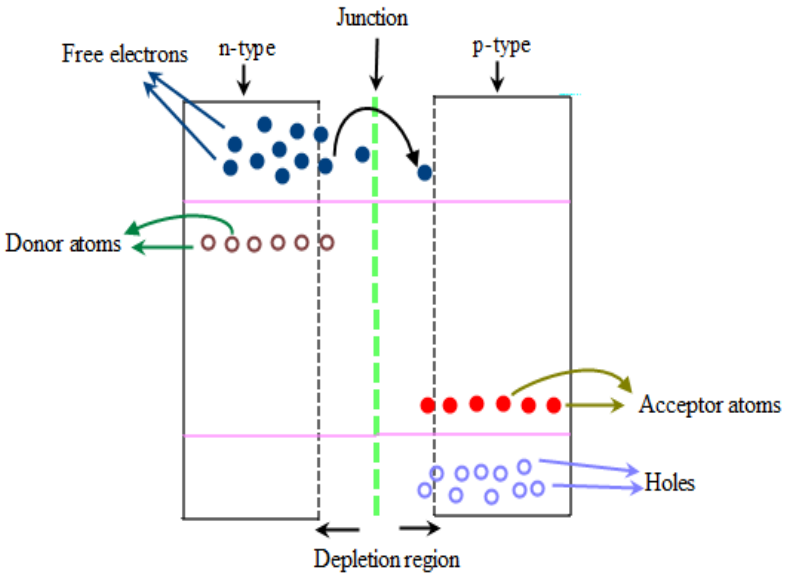

Figure 2. 3: Diagram of a crystalline solar cell

2.1.2 Charge Equilibrium

If both the electrons and holes arrive near to the junction, the electrons diffuse to the p-type region; similarly the holes diffuse to the n-type region and the cell hits to the charge equilibrium. This process deviates the ionized donors (acceptors) behind, generating a region around the junction, which is depleted of mobile transformers. This zone is called depletion zone and it extends from $X = -X_p$ to $X = X_n$. The charge due to the ionized donors and acceptors generates an electric field, which in turn causes a drift of transformers in the opposite direction. The diffusion of transformers goes on until the drift current (I_{drift}) equate the diffusion current (I_{diff}), attaining thus charge equilibrium as expressed by a constant Fermi energy. This occurrence is displayed in Figure 2.4.

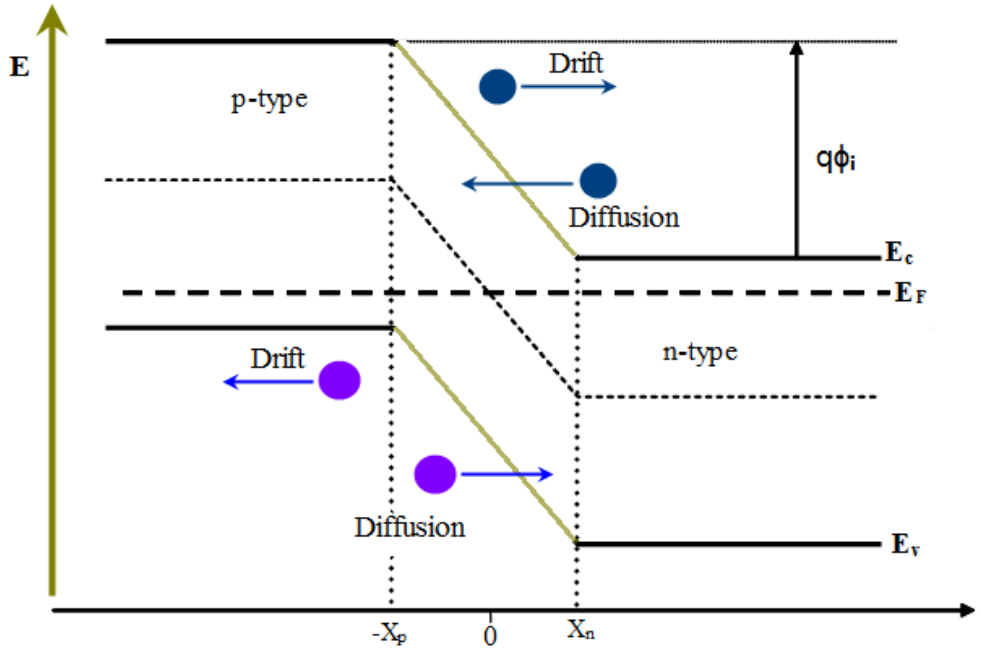

Figure 2. 4: Energy band gap of p-n junction in charge equilibrium

As shown in fig. 2.4 an internal potential ($q\Phi_{i)}$ is obtained by the difference between the n-type and p-type semiconductors. The potential across the depletion zone is resident internal potential in a semiconductor which is tended between -X_p and X_n. The following relation can be used to calculate the internal potential ($q\Phi_i$) [8].

$$\phi_i = V_f \ln \frac{N_d N_a}{n_i^2} \qquad 2.1.2$$

Where,

N_a : density of acceptor in the p-type zone per cm^3

N_d : Amount of donors in the n-type zone per cm^3

n_i^2 : Amount of positive or negative charge transformers per cm^3

V_f : k_bT/q (in volts)

k_b : Bolzmann's constant 1.38 x 10^{-23} JK^{-1}

k_bT : Kinetic energy (in eV)

q : an electron charge is 1.602x10^{-19} C

2.2 Dye Sensitized Solar Cell

The photoelectrode is a porous oxide semiconductor coated on conductive substrate. The conductive substrate is usually a soda lime glass deposited by thin layer of transparent oxide semiconductor, in general florin doped tin oxide (FTO) or indium tin oxide. After that, the produced film is sensitized bye oxidized dye and this sensitized film is called working electrode. On the other hand, A Platinum

film is deposited on ITO coated soda lime glass and this produced film is called counter electrode. The Pt film is necessary onto ITO because it increases charge transfer kinetics between ITO and I^- / I_3^- redox couple. It is known that the redox couple oxidation-reduction reaction is irreversible at bare ITO. The dye sensitized solar cell (DSSC) is fabricated by means of sandwiching the working electrode and counter electrode to each other, and filling the porous of TiO_2 layers by hole conductor. The schematic diagram of dye sensitized solar cell is shown in Figure 2.5.

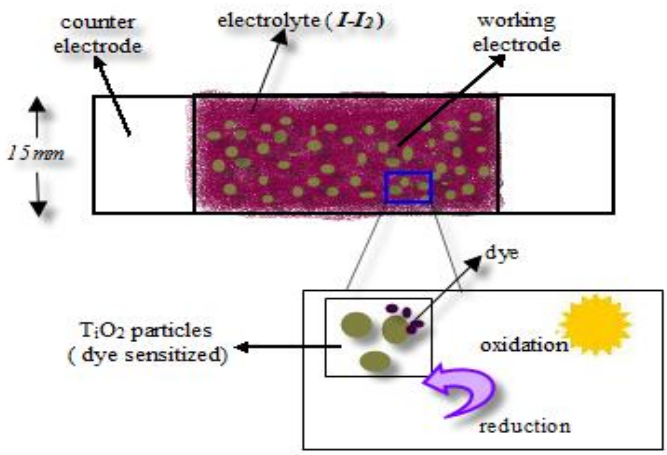

Figure 2. 5: Building of dye sensitized nanocrystalline TiO_2 solar cell

At the liquid cell, the hole conductors are obtained by redox system which are iodide and tri-iodide (I^- / I_3^-) couple in organic solvent. In addition to TiO_2 other semiconductor materials such as ZnO, SnO2, and Nb_2O_5 have been investigated as alternatives but the TiO_2 gave the best result so far in terms of efficiency. The oxide semiconductor TiO_2 as an electrode is ideal for the optical application because of its large band gap and absorbance at wavelengths below

400 nm. Therefore, the main part of the solar spectrum is available for absorption by the dye molecules.

2.3 Working Principle of Dye Sensitized Solar Cell

The operating principle of the dye sensitized solar cell (DSSC)is depicted in Figure 2.6 schematically. At the main of the system is a mesoporous oxide semiconductor composed of nano-sized particles which is sintered together to allow for electronic conduction to carry out. In general, the TiO_2 oxide semiconductor is used in the DSSCs while, the ZnO and Nb_2O_5 oxide semiconductors which have wide energy band gap can be studied alternatively.

The charge transmission dye is deposited to the surface of the nanocrystalline film (TiO_2). The working principle of dye sensitized solar cell involves three main processes. First process is the light absorption which happens in dye molecules. Second process is the charge separation by the electron injection from dye molecules to the conduction band of TiO_2 this step occurs at the interface of TiO_2 layer-electrolyte. Third process is the charge recombination. After the charge separation, the electrons flow through to the external load and they arrive to the counter electrode. The original form of the dye is immediately restored by electron donation from the electrolyte which is an organic solvent composed redox system, for instance the iodide/tri-iodide (I^- / I_3^-) couple. The regeneration of the sensitizer (S) by iodide (I^-) intercepts the recapture of the conduction band electron by the oxidized dye. The iodide is regenerated in turn by the reduction of tri-iodide (I_3^-) at the counter electrode the circuit being accomplished via electron travelling through the external load. As a result, the

DSSC cell produces a photo-current from light without suffering any perpetual chemical transformation. It should be repeated the redox reaction several times to achieve a continuous current on dye sensitized solar cells consistently. It was measured that the $Ru(dcbpy)_2(NCS)_2$ based TiO_2 solar cell performs 10^7 cycles without lowering performance in studies of Grätzel and his group [9].

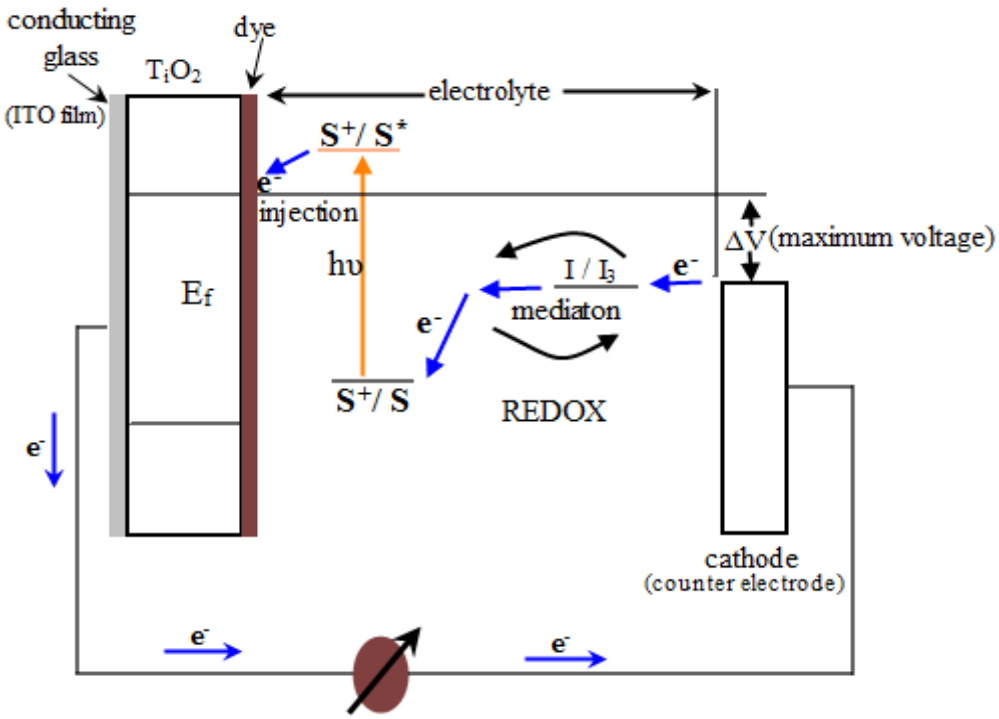

Figure 2. 6: Building of dye sensitized nanocrystalline TiO_2 solar cell

The formation of redox reactions in DSSC are given as above,

$S + h\upsilon \rightarrow S^*$ Absorption (2.3.1)

$S^* \rightarrow e_{cb} + S^+$ Injection of electron (2.3.2)

$S^+ + A^- \rightarrow S + A$ Regeneration (2.3.3)

$A + e^- \rightarrow A^-$ (2.3.4)

The maximum photo-voltage of DSSC can be obtained from Gibbs Free Energy differences between the psö-fermi level under radiation of TiO_2 and the redox potential of electrolyte.

2.3.1 Load Circuit Voltage

Throughout photo excitation of the dye molecules which is traditionally an organometallic sensitizer compound based on ruthenium (*S*), the electrons inject into the conduction band (CB) of the oxide semiconductor film (TiO_2). The absorption of the light occurs about a 720 nm for most dyes which are used in DSSCs. The electrons stream through the oxide semiconductor and they leave at the working electrode (it is explained in section 3.2) contact then they flow through an applied external load, after that the electrons react with the adsorbed oxidized half of the redox couple (iodide/tri-iodide) where between the interface of counter electrode-electrolyte. However, the electrons which are injected to the conduction band of the oxide semiconductor can undergo annoying surface recombination with either the oxidized half of the redox couple in solution or with the oxidized dye molecules. The high concentration of I^- ions that are present in

the cells, results in the fact that recombination of injected electrons with the dye molecules can be neglected [10].

According to the reactions (detailed in section 2.3) in DSSC, the incoming photon is absorbed by the dye molecules which are adsorbed on the nanocrystalline TiO_2 particles and then an electron from a molecular ground state (*S*) is excited to a higher lying excited state (*S**). The excited electrons are injected into the conduction band of the TiO_2 nanocrystalline film resulting in changing the ruthenium in the dye molecule in an oxidized state.

The injected electrons stream from conduction band of mesoporous TiO_2 film to the conductive layer of the soda lime glass (anode). Then, the electron flows through an external load back to the counter electrode (cathode). After that, the electron where in the counter electrode is transferred to the tri-iodide (I_3^-) to obtain iodide, and the cycle is looped by reduction of the oxidized dye and the iodide (I^-) which is then formed back to the tri-iodide (I_3^-) in the electrolyte. If the electrons can reach from the anode to the tri-iodide, the recombination which composed tri-iodide can occur at the interface of the oxide semiconductor-electrolyte [12,13]. A potential difference between the working electrode and the counter electrode is obtained due to the energy levels in the mechanism (see fig. 2.6). The Platinum (Pt) which is on the counter electrode behaves as a catalyst for the regeneration of the electrolyte. In addition, the maximum theoretical value for the photo-voltage can be determined by the potential difference between the conduction band of the TiO_2 and the redox potential of iodide-triiodide couple at load circuit condition [14]. As a result, there is no consuming of chemical matters

and no obtaining any chemical substances due to the working principle of the DSSC is in nature. In the abstract, the DSSC should be able to last forever.

2.3.2 Light Absorption

While the high efficiency of the dye sensitized solar cell arises from a collective effect of numerous well-tuned physical-chemical nanoscale features as will become apparent later, the key issue is the principle of dye sensitization of large band gap semiconductor electrodes. Moreover, in the DSSC this is over came by coating the internal surfaces of the porous TiO_2 electrode with essential dye molecules adjusted to absorb the incoming photons. The less absorption capacity of the dye became one of the challenges throughout the early improvement of the DSSC. The incident light is absorbed by the dye which on the layer of oxide semiconductors was less than 1%. When more dye layers are coated on the layer of the oxide semiconductors (TiO_2), not all the dye layers in interaction with the layer of TiO_2, therefore, the efficiency of DSSC was not reach to desirable levels. A nanoporous layer of TiO_2 with a surface area of nearly $300m^2/g$ (previously $10m^2/g$) was improved to accomplish this problem [15].

The efficiency of the dye sensitized solar cell depends on a cooperative effect of numerous physical and chemical nanoscale features. The main subject is the process of dye sensitization of the oxide semiconductor electrodes which have wide band gap. This problem is succeeded by deposition the inner TiO_2 electrode with dye molecules that can absorb the incoming photons.

2.3.3 Charge Recombination

The probability of direct recombination between the oxidized dyes and TiO_2 electrons may be a significant progression that limits the performance of photo-electrochemical cells [12]. It is calculated that the dynamics of charge recombination where between the oxidized dye and electrons of the TiO_2 are faster than re-reduction of the oxidized dye by I^- ions. This phenomenon would assert that for cell output voltages are larger than 0.6 V so, the direct recombination between the oxidized dye and the inner electrons of TiO_2 can result an important loss of photo-current. As a result of the redox potential of the redox couple (I^-/I_3^-) is nearly 0.2 V, the cell output voltage becomes 0.6 V that corresponds to a Fermi level of the TiO_2 electrode is -0.4 V. The recent models of the electrical performance of photo-electrochemical solar cells supposes that the recombination pathway is negligible and attributed to the loss of current at high output voltages merely to regeneration between the I_3^- ions and electrons of oxide semiconductor TiO_2 [12].

The charge recombination at the interface of nanocrystalline structure-redox electrolyte is anticipated to play an important role in lowering the photo-voltage [16]. There are two similar recombination pathways happening at the interface of nanocrystalline structure-redox electrolyte. The injected electrons from dye molecule to conduction band of TiO_2 may recombine with oxidized dye molecules or react with the redox species in the electrolyte. The contribution of the energy loss to the recombination current can generally be neglected due to the rapid rate of reduction of the dye molecules by the I^- ions which are existent at high concentration [17]. The iodide does not contribute to the diffusion impedance

due to the large excess of iodide relative to tri-iodide, and the diffusion constants of iodide and tri-iodide being of the same value [18,19].

2.3.4 Electron Flowing and Lifetime

The recombination of electrons which are in the conduction band of TiO_2 with the holes in the electrolyte such that I_3^-, is the most important loss system in the DSSC. The electron carriage by diffusion in the nanocrystalline TiO_2 and their recombination with the electrolyte are the two rival processes in the DSSC [20]. Figure 2.7 depicts the reaction paths at the TiO_2 interfaces.

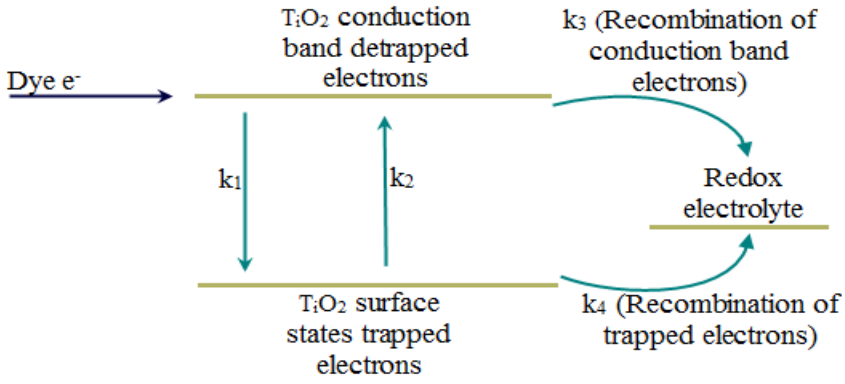

Figure 2. 7: Reaction paths at the TiO_2 interfaces in a DSSC

The reaction paths at the TiO_2 where following k values are characterized as below;

k_1, for the trapping of the TiO_2conduction band electrons (k_1 is about 10^3 times faster than k_2) [21].

k_2, for the detrapping of the electrons;

k_3, for the recombination of TiO_2 conduction band electrons;

k_4, for the recombination of trapped electrons.

Intensity modulated photo-voltage spectroscopy (IMVS) measurements exhibit that the rate of reverse reaction of photo injected electrons with I_3^- is second order in total electron concentration [21, 22]. This phenomenon is in correspondence with possible back reaction mechanisms of the electrons where in the nanocrystalline TiO_2 layer with the electrolyte, i.e. tri-iodide [16]. In addition, [16] used the second order back reaction both for the conduction band electrons and for the trapped electrons. The trapped electrons are on the TiO_2 layer just below the conduction band of the nanocrystalline TiO_2 and they are not available for reaction or migration. The trapping process is about 10^3 times faster than detrapping process therefore, almost all photo injected electrons are placed in trap or surface states rather than in the conduction band of TiO_2 [21]. Thereby, the recombination of conduction band electrons with the electrolyte ($k_3\ n^2$) can be omitted in comparison to the recombination of trapped electrons ($k_4\ N^2$), n and N denote the excess electron densities in the conduction band of TiO_2 and the trap states, respectively. A recombination of electrons in the TiO_2 layer with the oxidized dye under load-circuit situations is also negligible [12]. This recombination specimen permits for the description of effective transference parameters [27]. The effective lifetime of the electrons and the diffusion constant are determined by equation 2.7.1.

$$\tau_{eff} = \frac{1}{2N_0 k_4} \quad , \quad D_{eff} = D\frac{k_2}{k_1} \qquad 2.7.1$$

Where,

N_0 denotes the steady-state electron density in trap states.

D_{eff} denotes the effective electron diffusion constant in conduction band of the TiO_2 ($m^2\ s^{-1}$).

D is the electron diffusion constant in the bulk TiO_2 ($m^2\ s^{-1}$).

τ_{eff} refers the effective lifetime of the electrons.

The rate constants for charge injection into the conduction band of TiO_2 and the iodide reduction are at least 109 times higher than the rate constants for excited and oxidized state degradation [23]. The sensitizer should be able to undergo about one billion cycles without substantial degradation to be suitable as a dye for the lifetime of a cell. Several studies carried out regarding the stability of the dye, the electrolyte, the redox couple, and the sealing of solar cells. The Ru(*dcbpy*)$_2$(NCS)$_2$ dye has been validated for a commercial application. Moreover, light soaking experiments on photovoltaic devices have demonstrated the long period stability of Ru(*dcbpy*)$_2$(NCS)$_2$ dye at different temperatures. The liquid electrolyte can be encapsulated for several years under thermal cycling with the suitable sealing material inert to tri-iodide chemically [26].

On the other hand, the rate constant for electron injection from the excited state to the conduction band of the TiO_2 particles is in term of femtosecond (100 fs). The Ru(*dcbpy*)$_2$(NCS)$_2$ dye can undergo photo-induced loss or exchange of the thiocyanate ligand much lower than $105s^{-1}$ [24].

As well as the electron travelling in the TiO_2 electrode and the electron back reaction with the redox electrolyte is strongly influenced by trapping and detrapping effects thereby, this phenomenon is indicated by the very low values of the diffusion coefficient ($10^{-4}cm^2s^{-1}$). The electron migration and back reaction are defined in terms of the electron diffusion length $Ln = (D_n\tau_n)^{1/2}$, where D_n denotes the electron diffusion coefficient and τ_n denotes the electron lifetime [21].

In addition, the main factors limiting of the electron flowing are interparticle electron hopping and intraparticle ohmic resistance [25].

2.4 Dyes

There are different types of dye for use in construction of dye sensitized solar cell. So far, known dyes are polypyridyles [27], porfyrins [28,29], phatalosiyanins [30], coumarins [31,32], indolins, conjugated polymers, perylens [33]. However, rutenium polypyridyl complexes have been given the best performance so far. When the nanocrystalline TiO_2 dye sensitized solar cells were brought up in 1991, the dye which is $Ru(dcbpy)_2(NCS)_2$ and its derivatives became focus point. The $Ru(dcbpy)_2(NCS)_2$ dye is also known as black dye or N3. Even though ruthenium polypyridyle dyes have the most highly efficient, they are not ideal dyes. They have some disadvantages such as, its synthesis is difficult, it is expensive, its molar absorption coefficient is low and it is carrying out absorption in narrow range of sun's spectrum. The dye which is adsorbed on the nanocrystal grains of TiO_2 must have basic properties to provide transformation of high light energy to electrical energy. The properties of the dye can be ordered as below.

- ***Absorption:*** The dye should perform absorption in range of visible region (400-700 nm). In this case, the dye has a band gap 1,35 eV.
- ***Energy Values:*** Excited state energy of the dye must be slightly above of conduction band of TiO_2 and the energy difference must be sufficient to allow the transformation of electrons. So the losses of energy are reduced and the photo-voltage is kept as possible highest degree. In addition, the ground state energy level of the dye must be slightly below of redox potential of electrolyte.
- ***Stability:*** The dye which is adsorbed on surface of TiO_2 must be stable a long time (about 20 years) at working conditions (interface of semiconductor-electrolyte).
- ***Features of Interface:*** It must be perform a strongly adsorption on surface of used semiconductor.
- ***Application Properties:*** The dyes must have a high solubility and they must contain binding group to hold on to surface of semiconductor.

The adsorption of the dye to the semiconductor surface generally takes place via special anchoring groups attached to the dye molecule. These are thefour carboxylic groups (COOH) at the end of the pyridyl rings in the N3 dye. The COOH groups form a bond with the TiO_2 surface by donating a proton to the TiO_2 lattice [34]. The area occupied by one N3 molecule at the TiO_2 surface at full monolayer coverage is 1.65 nm^2 [34]. The efficient spectral sensitization in the DSSC is made apparent in Figure 2.8, where the spectral response curves, i.e. the photon to current efficiency curves, for cells sensitized with different dyes is compared with a bare TiO_2 electrode. The definite sensitization effect can be seen in Figure 2.6 as a shift of the incident photon to current efficiency (IPCE) curve of

the bare TiO_2 to the higher wavelengths when deposited with the N3 dye. The current efficiency of the cell is related to the 'height' of the IPCE curve, which depends on the charge separation and charge collection efficiencies. The IPCE curves in Figure 2.8 are not corrected for the optical losses in the soda lime glass, which only makes the obtained peak IPCE values more important.

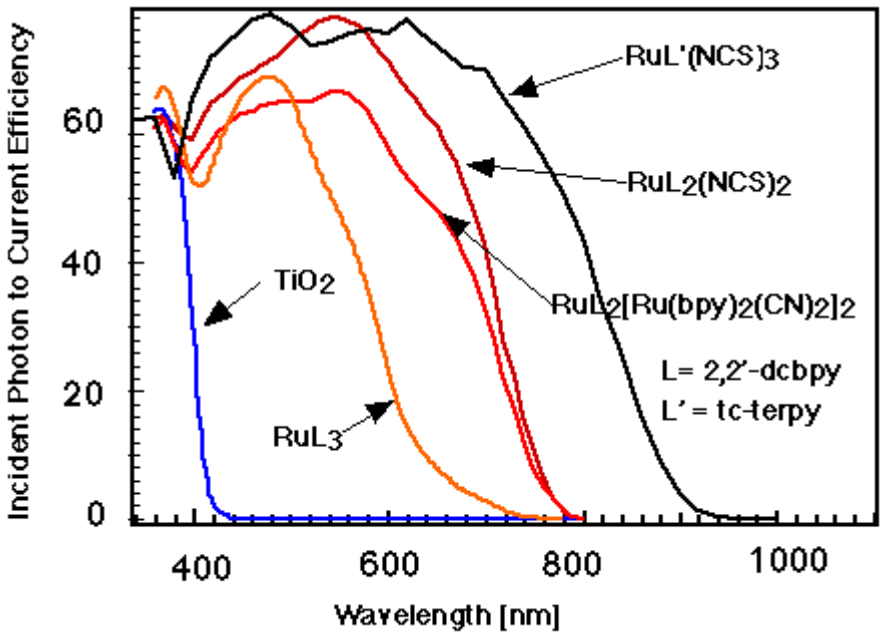

Figure 2. 8: Spectral response (IPCE) of dye-sensitized solar cell for different dyes compared with the spectral response of bare TiO_2 electrode and the ideal IPCE curve for a single band gap. Image from http://dcwww.epfl.ch/icp/ICP-2/solarcellE.html.

2.4.1 Molecular Structure of Dyes in DSSCs

There are four main type dyes for sensitization of the solar cells. Derivatives of perilendiimid (PDI), perilenmonoanhidrit (PMA) and perylene-monoimide (PMI) can be named organic dyes. On the other hand, complexes of ruthenium bipyridine are defined as organometallic dyes. The molecular structure of dyes is shown in Figure 2.9.

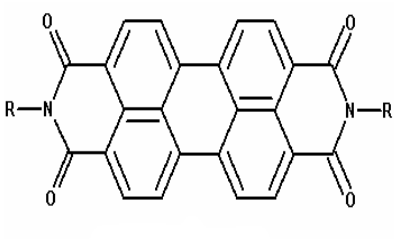

Perilendiimid (PDI)

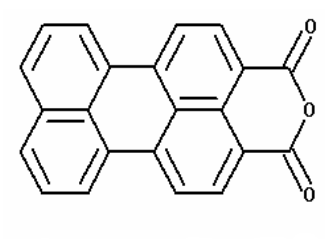

Perilenmonoanhidrid (PMA)

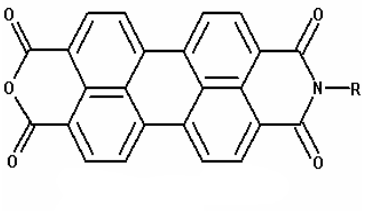

perylene-monoimide (PMI)

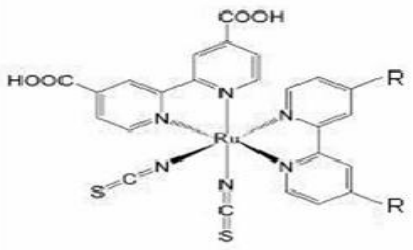

Ruthenium bipyridine

Figure 2. 9: Molecular structures of dyes in DSSC

2.5 Nano-crystalline Electrodes

2.5.1 Oxide Semiconductors

Oxide semiconductors are preferred in electrochemistry because they have stability against to photo-corrosion in situation of their exciting band gap. Oxide semiconductors which have large band gap ($E_g > 3$) should be used for providing transparency in visible region of the oxide semiconductor in the fabrication of dye sensitized solar cells. Some oxide semiconductors are used in production of nanocrystalline dye sensitized solar cells outside of TiO_2 as ZnO, SnO_2, CdS, CdSe, WO_3, Fe_2O_3, Nb_2O_5, Ta_2O_5 however, the TiO_2 continuous to be most popular semiconductor.

2.5.2 TiO_2 Semiconductor

Titanium dioxide or titania (TiO_2) film is one of the most widely studied transition-metal oxides. During the past few decades, the TiO_2 films have attracted great attention for their potential applications in physical, optical, electrical, photocatalytic and electronic fields [35–45]. A variety of techniques such as chemical spray pyrolysis [46], chemical vapor deposition [45, 46], sol–gel [49], sputtering [40, 50], and electron-beam evaporation [51, 52] have been used to prepare high quality TiO_2 thin films. The conventional spray pyrolysis methods, among others, are the most preferred technique owing to the reproducible deposition of the films accomplished quite easily compared to the other methods.

The TiO_2 film exhibits three distinct polymorphs: the rutile phase tetragonal, the anatase phase tetragonal and the brookite phase orthorhombic. Among these phases, although the rutile structure is the most common in nature, the anatase structure is usually used as photocatalyst because of the large optical band gap energy, about 3.2eV, related to an indirect band to band electronic transition [53, 54]. As well-known less electron–hole recombination is observed in indirect band gap materials, leading to the use of the anatase structure as wide band gap semiconductor, specifically for the charge separation in dye-sensitized solar cell [54, 55]. Nevertheless, the large band gap limits the photocatalytic efficiency of the TiO_2 film under sunlight irradiation due to the use of only 2–3% of the UV light in the total solar spectrum for water splitting. Several methods such as the chemical doping (metals, rare elements, nitrogen or iron), and the change of annealing conditions and sputtering parameters have therefore been

studied to increase both the photocatalytic efficiency of the TiO_2 structures [56, 57] and the surface area and the surface hydrophilicity [58]. The required surface area and hydrophilicity properties of the TiO_2 film are obtained from the small grain/particles size in anatase structure, resulting in a not only more efficient light and water absorption but higher photoefficiency and photocatalytic activity [59], as well.

2.5.3 Indium Tin Oxide (ITO)

Since the discovery of the transparent conducting oxide (TCO) films, researchers have endeavored to develop their electrical, optical and microstructural properties to make them suitable for the advanced technological devices such as solar cells, light emitting diodes, photodiodes, photo- catalysts, optical memories, flat panel displays, gas sensors, energy efficient windows, storage-type cathode ray tubes, surface layers in electroluminescent applications [60–68]. Indium tin oxide (ITO) films are the most promising materials for the potential technological and industrial applications including solar cell, liquid crystal displays and photo-detectors, etc. [69–72] because of the higher optical transparency, lower resistivity, chemical stability, excellent adhesion and etching properties compared to other transparent and conducting oxide films such as TiO_2, SnO_2 or ZnO [73-77]. As well known, the ITO material behaves as an insulator in its stoichiometric form while the material is a conductor in the non-stoichiometric form with a wide direct optical band gap of 3.6 eV [78], resulting from the formation of a conducting carrier-oxygen vacancies with the addition of a dopant tetravalent cation Sn^{+4} to the matrix In_2O_3. Thus, the oxygen vacancies acting as doubly- ionized donors contribute maximum two electrons to the electrical

conductivity in the sample [79]. As a result, the conductivity of the ITO sample changes. The preparation conditions such as the operational procedures, annealing ambient (time, temperature atmosphere and pressure), composition, type and quantity of the dopant and heat treatment method also affect the level of the conducting carrier concentration and oxygen vacancies. In particular, the annealing ambient plays a very significant role on the fabrication of the high quality ITO films. It is argued that the crystallinity of the ITO thin films improves with the post-deposition annealing temperature because of the decrement in the structural defects [80–83]. In other words, the variation of the optical and electrical characteristics for the ITO thin film studied stems from the changes in the local ordering of the material during crystallization and the oxygen vacancy creation [75]. In order to prepare high quality ITO film, several deposition techniques such as thermal evaporation, chemical vapor deposition, electron beam evaporation, sol–gel, spray pyrolysis, pulsed laser deposition and magnetron sputtering have been experienced for years [84–88]. The conventional sputtering methods, among others, are the most preferred technique due to the reproducible deposition of the films accomplished quite easily compared to the other methods [89].

CHAPTER 3

EXPERIMENTAL DETAILS

3.1 Coating of Conducting ITO Layer by DC Sputter Magnetron

Deposition of the ITO thin films on soda lime glass was carried out by DC magnetron sputtering system as shown in Figure 3.2 (NSC–3000 DC Sputter Machine) using an oxide ceramic target composed of 90wt% In_2O_3 and 10wt% SnO_2. Prior to the film deposition process, all the substrates were ultrasonically cleaned by acetone, degreased in a dilute detergent solution, rinsed thoroughly with deionized water and blown dry in nitrogen flow. In addition, the active area of substrates was 1.5x2.5cm. ITO disk (99.99 % pure) with a 50 mm in diameter and a 4 mm in thickness was used as sputtering target. The substrates were vertically placed onto the substrate holder and the distance between them was adjusted to be about 60 mm. The chamber was evacuated down to a pressure lower than 10^{-6} Torr and the sputtering process was performed in 99.999 % pure argon (30sscm for sputtering gas) at a DC power of 100 W. During the deposition, the substrates were kept at room temperature for 10 min. The ITO films removed from the sputtering system were exposed to the calcination process at different temperature and time in the tube furnace (Protherm- 121 Model PTF12/75/200) as shown in Figure 3.1. The best annealing ambient for the fabrication was determined to be 400 °C for 2 h.

Figure 3. 1: Image of furnace

Figure 3. 2: Image of DC Sputter

3.2 Preparation of TiO_2 Film by Spray Pyrolysis

Titanium dioxide films were deposited on the ITO surface of soda lime glass (defined in section 3.1) by spray pyrolysis method. Firstly, the solution of Titania (TiO_2) was prepared by this way: 5.76 mL titanium (IV) isopropoxide was solved in 90.26 mL ethanol. Then, a few drops of acetonic acid was added to the solution and the solution lasted in dark media for 30 min. thus, the solution is ready for coating on the ITO surface of soda lime glass. Then, several experiments were carried out to determine the best annealing environment for the fabrication of the TiO_2 thin film on the ITO surface.

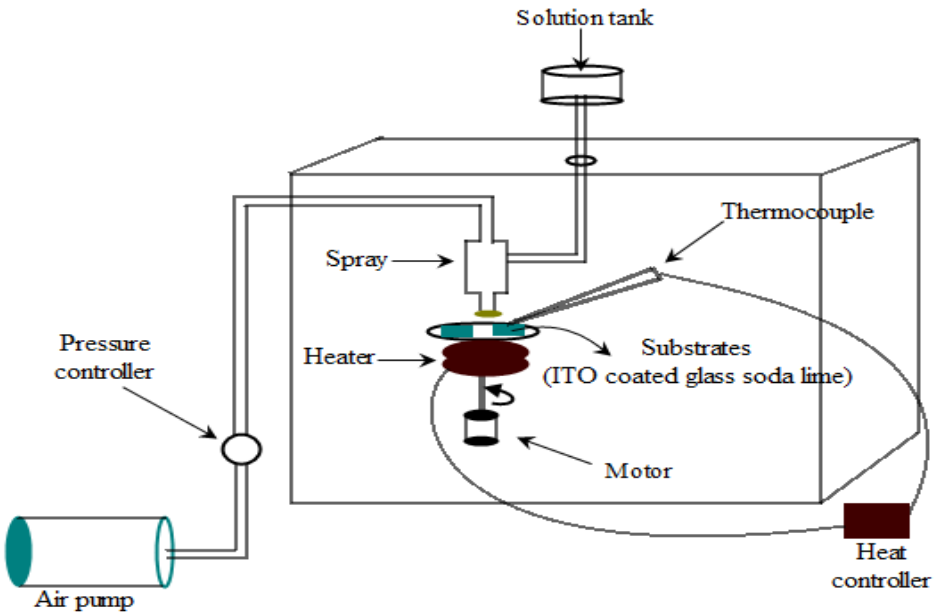

Figure 3. 3: Schematic diagram of spray pyrolysis system

The schematic diagram of spray pyrolysis system is shown in Figure 3.3. The ITO substrate was placed on the substrate holder. Then the heater was set to

450 ^{0}C (the best annealing temperature) by the temperature controller, and the solution prepared was transferred to the solution tank. Second, the air pump was set to 1.5 atmosphere pressure by the pressure controller valve. After that, the motor which has 4 rotations per minute was turned on and the spray apparatus was aligned over the substrates by the distance of nearly 8 cm. The coating process was finished for half an hour. After coating process, the sample prepared was cooled at room temperature. The coated TiO_2 on ITO surface of soda lime glass is called working electrode.

- ***Preparation the Solution of cisBis(isothiocyanato)bis(2,2'bipyridyl4,4'-dicarboxylato)ruthenium(ıı) Dye***

In this work, molecular mass of the dye is 705.64 g and 40mL solution was prepared. The mass of dye is calculated by relations as given below;

$$M = \frac{n}{V} \quad , \quad n = \frac{m}{M_a} \qquad 3.2.1$$

where, M denotes molarity, n is mole, V represents volume, m shows mass of dye and M_a is molecular mass of the dye. For 40 mL solution, 8.468 milligrams of dye was solved in 40 mL ethanol, and thus $3x10^{-4}$ M solution was obtained. In addition, the molecular structure of cisBis(isothiocyanato)bis(2,2'bipyridyl4,4'-dicarboxylato)ruthenium(ıı) dye is shown in Figure 3.4.

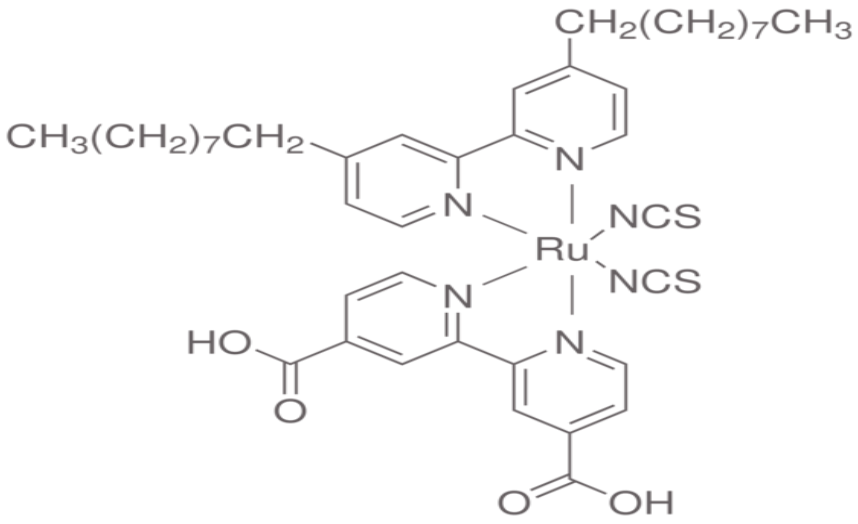

Figure 3. 4: Molecular structure of cisBis(isothiocyanato)bis(2,2'bipyridyl4,4'-dicarboxylato)ruthenium(II) dye

- **Preparation of 50 mM tri-iodide in acetonitrile (electrolyte I^- / I_3^-)**

2 g of potassium iodide and 1.3 g of I_2 were added into 100mL beaker. Then a few mL of acetonitrile was added and swirled for a few minutes until iodine was dissolved. After that, the iodine solution was transferred to a 100 mL volumetric flask and the solution was completed to the 100 mL mark with acetonitrile. In solution, the iodine will bind with iodide to obtain a tri-iodide in an equilibrium reaction with an equilibrium constant for formation, K_1:

$$I_2 + I^- = I_3^- K_1$$

When the iodine concentration is high, polyiodide species such as I_5^-, I_7^-, and I_9^- may also be occurred, but actually, only tri-iodide appears to be of importance in DSSC electrolytes. Because K_1 is high in the organic solvents typically used for electrolytes in DSSCs and the iodide concentration is high, the concentration of free iodine will be very low.

3.3 Preparation of Platinum Film

Coating of the Pt thin film on the surface of ITO soda lime glass was conducted by DC magnetron sputtering system (NSC–3000 DC Sputter Machine) using target composed of 90 wt% Pt. Prior to the film deposition process, all the substrates were ultrasonically cleaned by acetone, degreased in a dilute detergent solution, rinsed thoroughly with deionized water and blown dry in nitrogen flow. Moreover, platinum disk (99.99 % pure) with a 50 mm in diameter and a 4 mm in thickness was used as sputtering target. The substrate was vertically placed onto the substrate holder to obtain homogeneous distribution and the distance between them was about 60 mm. The chamber was evacuated down to a pressure lower than 10^{-6} Torr and the sputtering process was performed in 99.999 % pure argon (30sscm for sputtering gas) at a DC power of 75 W. During the deposition, the substrate was kept at room temperature for 4 min. The coated this thin film is called counter electrode.

3.4 Fabrication of Dye-Sensitized Solar Cell

In this study, the dye-sensitized solar cell was fabricated by the following steps;

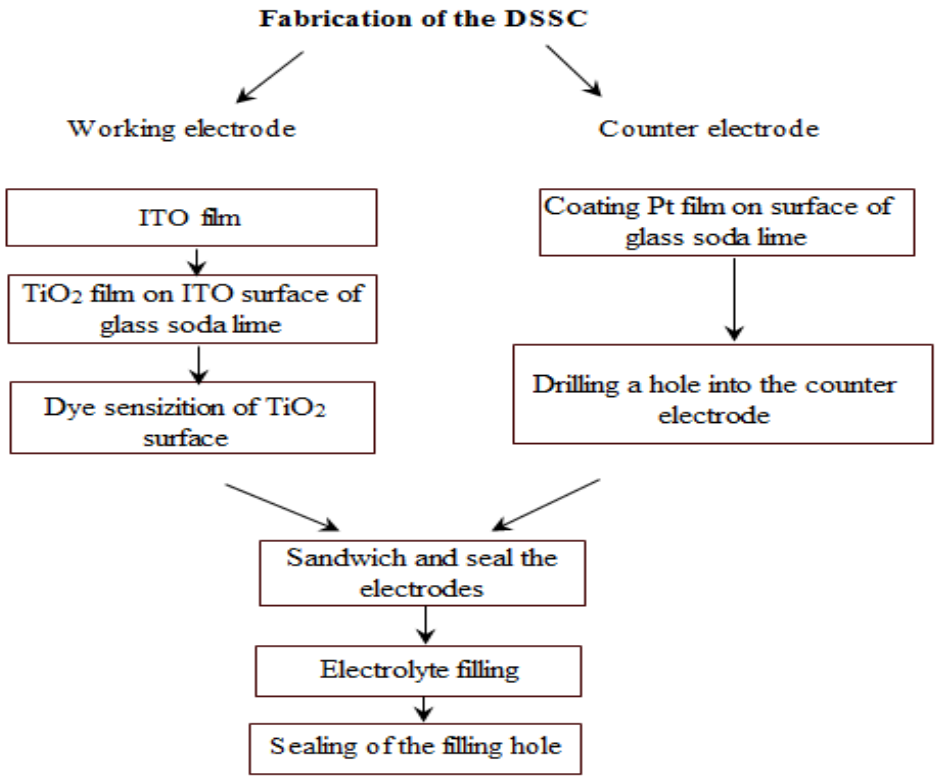

Figure 3. 5: Schematic diagram of fabrication of DSSC

As shown from Figure 3.5, after the ITO film was coated on surface of soda lime glass, the prepared solution of TiO_2 was sprayed on ITO surface of soda lime glass by spray pyrolysis method. Then, the film obtained was sensitized by waiting for 12 hours in the dye prepared in section 3.2. After the waiting process, the film was taken from the dye and washed with ethanol. This sensitized film is called working electrode. On the other hand, Pt film, coated on soda lime glass substrate by DC sputtering method, is called as the counter electrode. A small

hole was drilled into the counter electrode to fill the electrolyte. After that, the working electrode and counter electrode were sandwiched to each other as shown in Figure 3.6. Finally, the electrolyte was filled from the drilled hole into the cell and the hole was sealed. As a result, the fabricated cell (Figure 3.5) is ready for measurements.

Figure 3. 6: Image of the fabricated DSSC

3.5 XRD and UV-VIS Measurements

The crystal structures of the ITO and TiO_2 films studied were characterized by means of a Rigaku Multiflex XRD with CuKα radiation (λ=1.5418 Å) in the range 2θ=20–60° at a scan speed of 3°/min and a step increment of 0.02° at room temperature. Furthermore, the average sizes of the crystal of the samples were estimated from the Scherrer–Warren approach by

utilizing from the broadening nature of the XRD peaks. Moreover, the transmittance spectra of the films were recorded in the wavelength range from 300 to 700 nm by a JASCO 430 UV–VIS spectrophotometer. The refractive index (n_λ), porosity and optical band gap energy values of the ITO and TiO_2 films fabricated are also computed with the aid of the transmittance spectra. The image of X-ray Diffractometer is presented in Figure 3.7.

Figure 3. 7: Image of X-ray Diffractometer

3.6 AFM Measurement

The microstructural properties and height asymmetries of the ITO and TiO_2 thin films were conducted using Atomic Force Microscopy (AFM) from Nanomagnetic Instruments. Morphological features of the films prepared are examined using AFM (Nanomagnetic Instrument). Topographic and phase images

were obtained in the non-contact mode under room conditions with typical rate of about 1 line per second with a resonance frequency of about 300 kHz. Measurements were performed with 512 scan lines. Several regions on the specimen surface were scanned to observe the similar images. AFM images analysis was carried out with special software written by Nanomagnetic Instrument group. Analysis was performed in the non-contact mode. Moreover, the AFM measurements were conducted with an imaging aspect ratio of 1:4 to minimize the signal distortion in the scan slow direction due to thermal drift. [99–101]. The image of Atomic Force Microscopy is illustrated in Figure 3.8.

Figure 3. 8: Image of AFM

3.7 SEM Measurement of TiO_2 Film

The scanning electron microscope (SEM) produces a beam of electrons in a vacuum. That beam is collimated and focused by electromagnetic lenses and scanned across the surface of the sample by electromagnetic deflection coils. The interaction of the primary electron beam with the material of the sample in SEM causes excitation of secondary, backscattered, Auger electrons, characteristic X-ray radiation and photons of light.

The primary imaging method is by collecting secondary electrons that are released by the sample. The secondary electrons are detected by a scintillation material that crops flashes of light from the electrons. The light flashes are then detected and amplified by a photomultiplier tube. By correlating the sample scan location with the resulting signal, an image can be designed that is similar to what would be seen through an optical microscope. There are other imaging modes available in the SEM. Backscatter imaging uses high energy electrons that emerge nearly 180° from the illuminating beam direction. The backscatter electron yield is a function of the average atomic number of each point on the sample, and thus can give compositional information. Specimen current imaging using the intensity of the electrical current induced in the specimen by the illuminating electron beam is used to produce an image. It can often be used to show subsurface defects.

The morphology of the TiO_2 film produced in this work is analyzed by using a Scanning Electron Microscope (SEM) JEOL 6390-LV, with an accelerating voltage of20 kV in the secondary electron image mode. The image of SEM is shown in Figure 3.9.

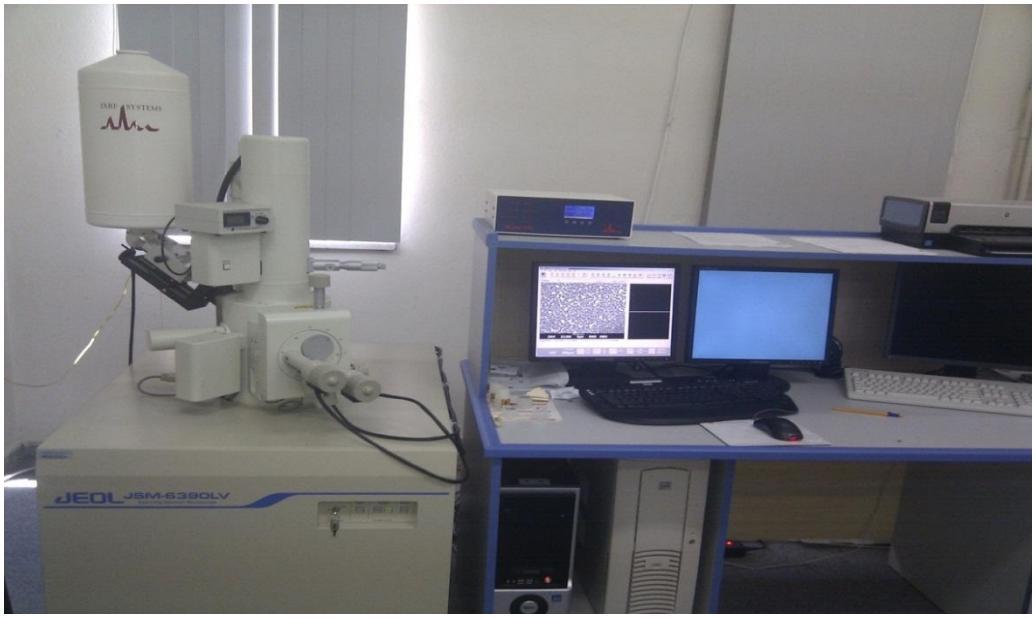

Figure 3. 9: Image of SEM.

3.8 Current-Voltage Measurement of the cell

When a dye sensitized solar cell is kept under an illumination, the current through the solar cell is balanced by an amount equal to the photo-current (I_{photon}), produced by the electron injection of the dye into the conduction band of the TiO_2 film. An instance of an I-V curve is shown in fig. 3.11. In order to scan the results of the cell in different areas, the current density (J) is used rather than the current (I). The efficiency of the cell (η) is signified by the open-circuit voltage (V_{oc}), defined as the voltage delivered by the cell when there is no external connection between the electrodes, i.e. the total current is zero. The short-circuit current density (J_{sc}), is defined by two electrodes that are short circuited, i.e. the voltage through the cell is zero. Further, the fill factor (FF) defined as the squareness of the I-V curve is determined by ratio between the maximum power output (P_{max}) and the product of V_{oc} and J_{sc}. After the fabrication of dye sensitized solar cell, I-V values of DSSC were measured with the system which is shown in fig.3.10.

First, an area called active area was established on the DSSC. Then, all connections were completed as shown in the fig. 3.10. Finally, the measurements were done at incoming illumination (P_{input}) of 1 kW/m^2 and active area of 4cm^2. The values of a current corresponding to a voltage were measured by changing the resistance value with the aid of the resistance box. The measurement was repeated several times to obtain more and more data.

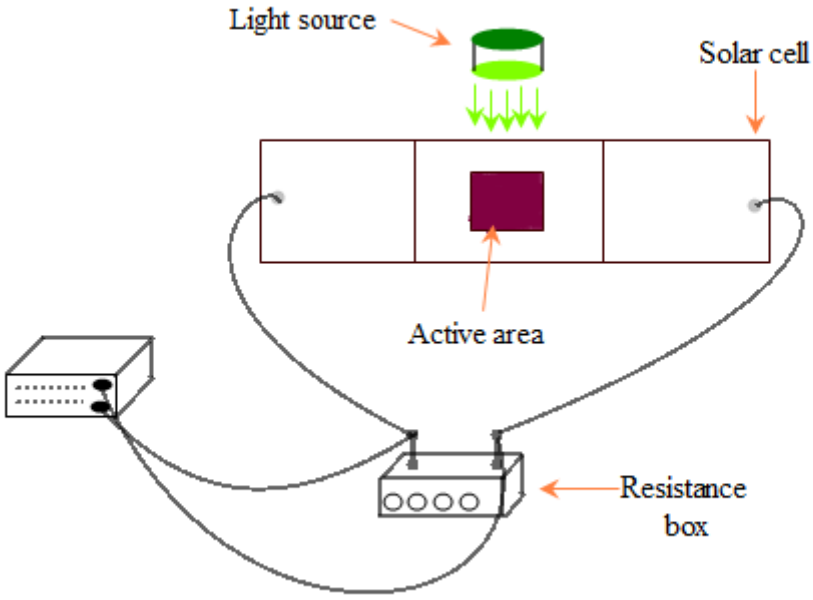

Figure 3. 10: Schematic diagram of I-V measurement of the cell.

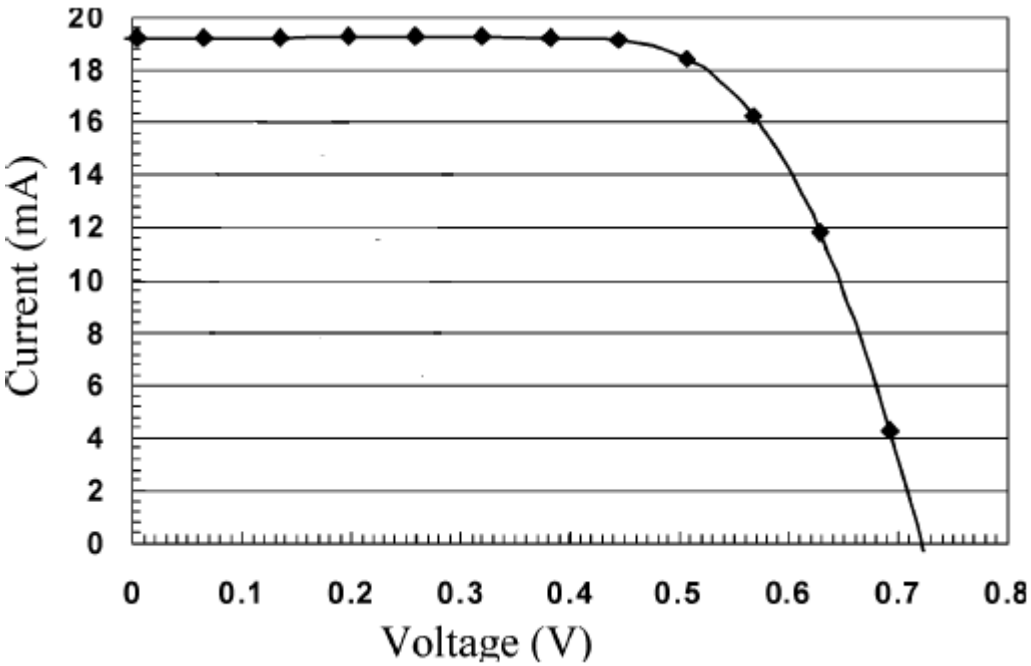

Figure 3. 11: Instance of I-V curve of a DSSC.

CHAPTER 4

RESULTS AND DISCUSSIONS

4.1 XRD Characterizations

4.1.1 XRD Patterns of TiO_2

Figure 4.1 indicates the XRD patterns between 20° and 60° for the TiO_2 thin film prepared. It is visible from the figure that the film produced in this work exhibited the polycrystalline superconducting phase with the changing intensity of diffraction lines and contained the anatase phase only. The anatase peaks are presented by A(*hkl*) Miller indices given in the diagrams. It is found that A(*101*) peak, among the peaks, has the highest intensity. Thus, the grain size of the film is determined from the A (*101*) peak using Scherrer's equation [90–93].

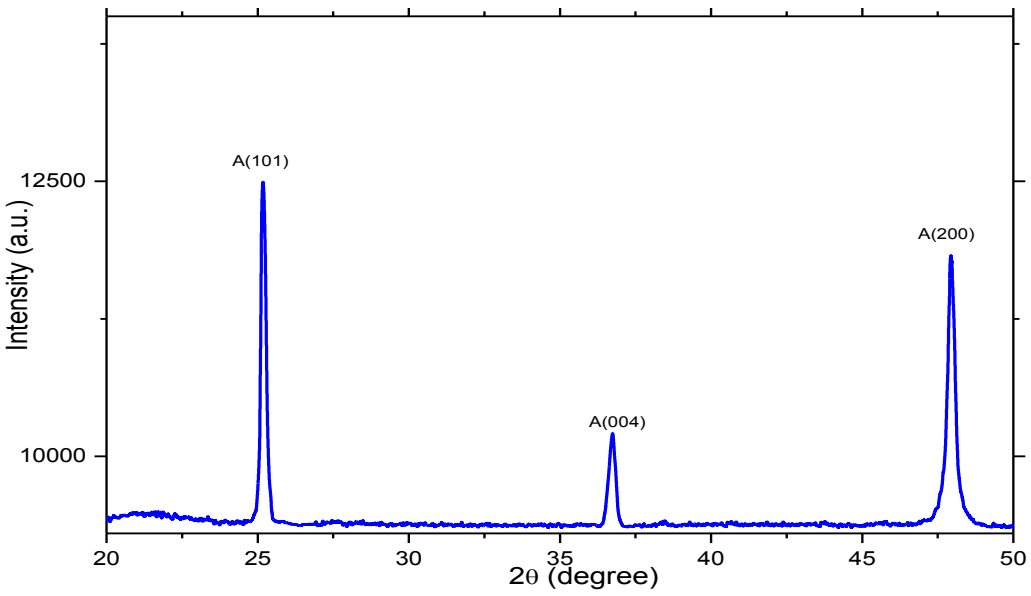

Figure 4. 1: XRD patterns of the TiO_2 (A shows anatase phase)

According to the equation, in broadening region the average size of a crystal is defined as;

$$d = \frac{0.941\lambda}{B\cos\theta_B} \qquad 4.1$$

where d is the thickness of the crystal, λ denotes the wavelength, B presents the full width half maximum (FWHM) of the Bragg peak corrected using the corresponding peak in micron-sized powder and θ_B is the Bragg angle, also. B is the line broadening, by reference to a standard, so that

$$B^2 = B_m^2 - B_s^2 \qquad 4.2$$

where B_s is the half-width of the standard material in radians. The calculation obtained is listed in Table 4.1. One can see from the table that the grain size of the TiO_2 film is nearly 45 nm.

Parameters	TiO_2 film
Grain size from XRD (nm)	45
Grain size from AFM (nm)	52

Table 4. 1: Results of TiO_2 thin film which was prepared on ITO surface of soda lime glass substrate

4.1.2 XRD Patterns of ITO

The XRD patterns between 20° and 60° for the ITO film grown on the soda lime glass substrate are shown in Fig. 4.2. The diffraction patterns obtained are used to determine the texture, grain size, interplaner distance, lattice constant and strain parameters for the sample. The corresponding (*h k l*) Miller indices belonging to the In_2O_3 main lines are shown in the diagrams. It is visible from the figure that the sample produced contains the In_2O_3 phase only and exhibits the polycrystalline and cubic bixbite structure with more intensity of diffraction lines, illustrating that the tin atoms are probably doped substitutionally into the lattice. Moreover, the film annealed displays a weak peak at 2θ=38.1° corresponding to (*411*) plane of In_2O_3. This phenomenon can be explained by the crystallization temperature (160–180 °C) of amorphous ITO films [94–96]. Additionally, the peak intensities including (*411*) and (*431*) are observed for the ITO film, confirming the coexistence of <*411*> and <*431*> textures. The peak (*222*) becomes very strong for the sample as a result of the preferred orientation in the direction of <*111*>, attributed to both the increment of the donor sites trapped at dislocations or point defects aggregates, and the decrement of the ITO film conductivity [97, 98]. The thermalized sputtered atoms favor to crystallize in (*222*) orientation whereas the high energy particles prefer the (400) and (440) directions in consequence of their energy. The strongest intensity of (222) peak is obtained for the ITO film annealed at 400 °C, showing that the ITO film has the fine crystallinity and largest grain size.

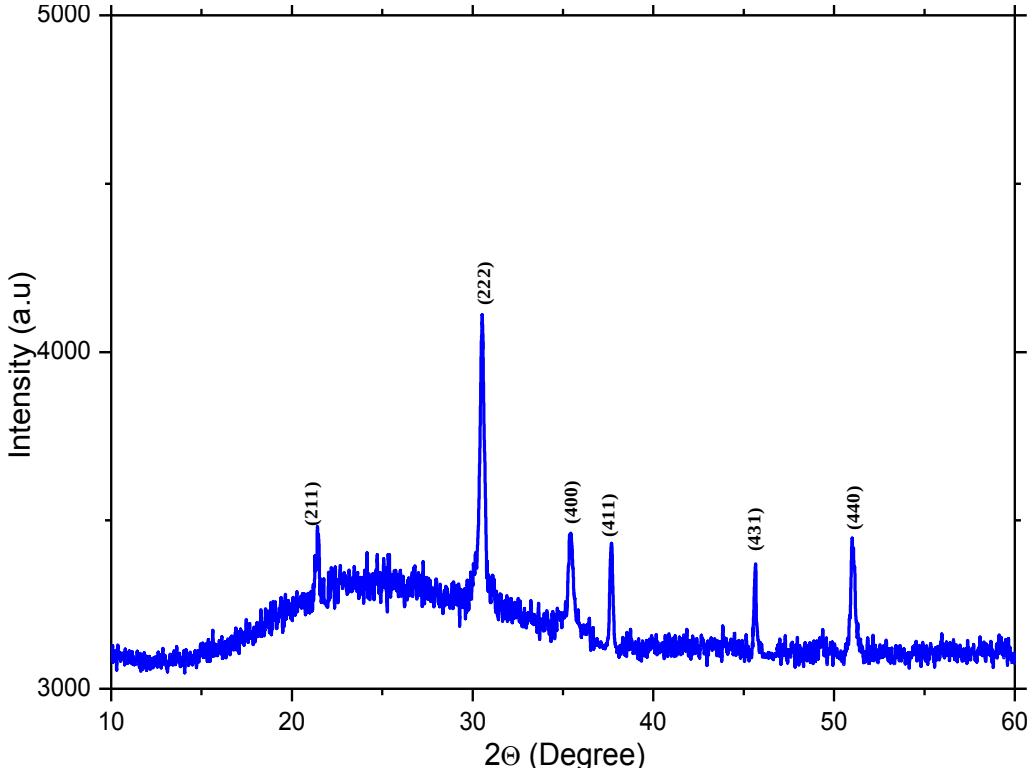

Figure 4. 2: X-rd of ITO

The ratio between the intensity of (222) peak to (400) peak qualified as the crystal quality parameter, (I_{222}/I_{400}) is calculated for the ITO film and the results obtained are listed in Table 4.2. It is apparent from the table that the parameter of the ITO film is about 2.80; however, it is well known that the standard value for ITO powder is 3.33 [99]. As understood, the ratio of the ITO film is found to be near the standard value of the ITO powder, showing that the layers of the annealed ITO sample obtain more oxygen vacancies, resulting in the (*222*) growth direction and the increment in the conductivity of the film. Moreover, the lattice constant (*a*) and interplaner distances (*d*) calculated by means of the peak (*222*) for the film is tabulated in Table 4.2. As seen from the table, all the parameters obtained are found to be larger than the ITO standard parameters as a result of the growth induced stress [100] which stems from the oxygen deficiency [101, 102]

and thermal expansion coefficient mismatch between the film and substrate [103,104].

Furthermore, the grain size of the ITO film prepared can be derived from the broadening nature of the XRD peaks following the Scherrer method [90–93]. The crystallite size is determined by the equation 4.2 and the result obtained show that the ITO film has large grain size (54 nm). According to the results, the ITO film has the fine crystallinity and connectivity between grains. As well known, the improvement in the crystallinity is attributed to a decrease of donor sites trapped at the dislocations and grain boundaries, and also to the out-diffusion of oxygen atoms from interstitial positions [105].

Main parameters	ITO film
$\frac{I(222)}{I(400)}$	2.688
Texture	<*111*>
Lattice constant (Å)[a]	10.129
Plane distance (Å)[a]	2.924
Grain size from XRD (nm)	54

(a) The standard values for ITO powder are: cell constant (a_0) = 10.118 Å [100] and plane distance: (d_0) = 2.921 Å [99].

Table 4. 2: XRD intensity ratios, I_{222}/I_{400}, texture, grain size, lattice parameter and plane distance for the ITO film

4.2 Surface Morphologies

4.2.1 Surface Morphology of TiO_2

Surface morphology of the TiO_2 film prepared in this study is conducted using AFM technique. Thickness, grain size, average roughness and rms roughness are important parameters to obtain about the microstructural properties of a thin film. Thickness and grain size values of the film are found with the aid of AFM image presented in Fig. 4.3. The obtained results are depicted in Table 4.3. One can observe from the table, the thickness value of the film is about 100 nm. Moreover, the grain size of 52 nm is obtained for the TiO_2 film, supported by the XRD result. Besides, average roughness parameter (S_a) is the arithmetic mean or average of the absolute distances of the surface points from the mean plane while rms roughness parameter (S_q) is the root mean square of the surface departures from the mean plane within the sampling area [106].

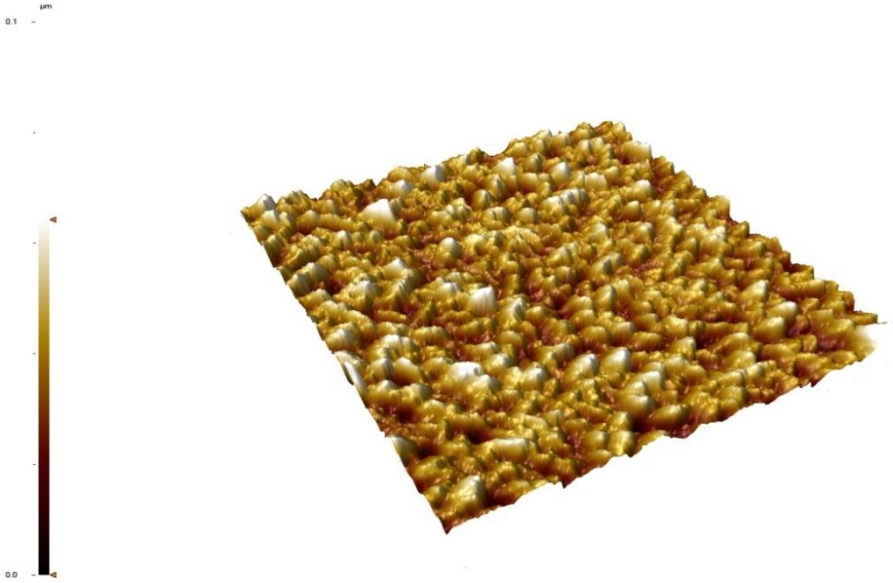

Figure 4. 3: Atomic Force Microscopy images of TiO_2 film deposited on ITO surface of soda lime glass substrate

Statistical Parameters	TiO_2 film
Average roughness (nm)	95.7
RMS roughness (nm)	98.5
Skewness, S_{sk}	1.076
Kurtosis, S_{ku}	1.201

Table 4. 3 Statistical parameters of the TiO_2

Average roughness parameters can be calculated by means of the following relation:

$$S_a = \frac{1}{MN}\sum_{j=1}^{N}\sum_{i=1}^{M}|z|(x_i, y_j) \quad 4.3$$

and rms roughness parameter can be calculated using the equation,

$$S_q\sqrt{\frac{1}{MN}\sum_{j=1}^{N}\sum_{i=1}^{M}z^2(x_i, y_j)} \quad 4.4$$

where *M* denotes the number of columns in the surface and *N* is the number of rows in the surface. The results obtained are given in Table 4.3. It is found that the TiO_2sample obtains fine surface roughness (S_a: 95.7 nm and S_q: 98.5 nm). According to these results, the regular structures were observed on the surface of the TiO_2 film studied. However, the different surface roughness values might show the possible reason for the variation of the oxygen in the samples studied.

The statistical analysis of AFM image is also carried out by using the height distribution histogram depicted in Fig. 4.4.

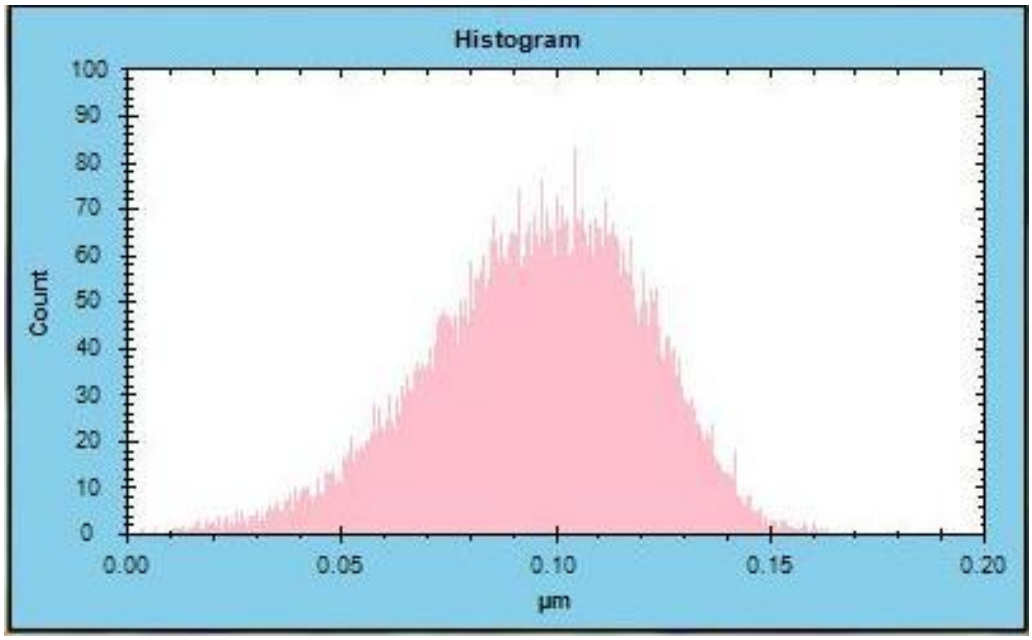

Figure 4. 4: Height distribution histogram of the TiO_2.

The height asymmetry can be explained by the surface skewness and kurtosis from the quantitative surface roughness parameters [107]. The surface skewness (S_{sk}) is a measurement for the symmetry of the variation of a surface about its mean plane. Whenever a Gaussian surface obtains a symmetrical shape for the height distribution, the surface skewness is zero. A plateau honed surface with predominant plateau and deep valleys tend to have a negative skewness whereas a surface comprised of disproportionate peaks obtains positive skewness value. The skewness can be computed from the following relation:

$$S_{sk} = \frac{1}{MNS_q^3} \sum_{j=1}^{N} \sum_{i=1}^{M} z^3(x_i, y_j) \qquad 4.5$$

On the other hand, the surface kurtosis (S_{ku}) is a measurement of the peakedness or sharpness of a surface. For a Gaussian surface, the kurtosis value is 3. If a surface is centrally distributed kurtosis value is greater than 3. When a surface has a well spread out distribution, the kurtosis value is less than 3. Kurtosis is calculated using the following equation:

$$S_{ku} = \frac{1}{MNS_q^4} \sum_{j=1}^{N} \sum_{i=1}^{M} z^4(x_i, y_j) \qquad 4.6$$

The surface skewness and kurtosis roughness of the samples are also listed in Table 4.3. It is apparent from the table that the surface skewness is obtained to be positive for TiO_2 while the surface kurtosis is found to be less than 3. According to the combination of the skewness and kurtosis values, the film surface is found to be spread out distribution and comprised of disproportionate number of peaks. Based on the interpretation of the surface morphology and statistical parameters, the TiO_2 film produced in this work can be useful for applications in technology and industry.

4.2.2 Surface Morphology of ITO

Atomic Force Microscopy (AFM) is useful method to both analyze the surface morphology of a thin film and obtain information about the thickness, roughness and height asymmetries values such as the skewness and kurtosis of the film [108,109]. The typical AFM image corresponding to the ITO film annealed at 400 °C is depicted in Fig. 5, respectively. The surface scanned is 5 × 5 μm. It is visible from Fig. 4.5 that the surface morphology appears regular and fine. The image of the ITO film illustrates great individual grains with less roughness.

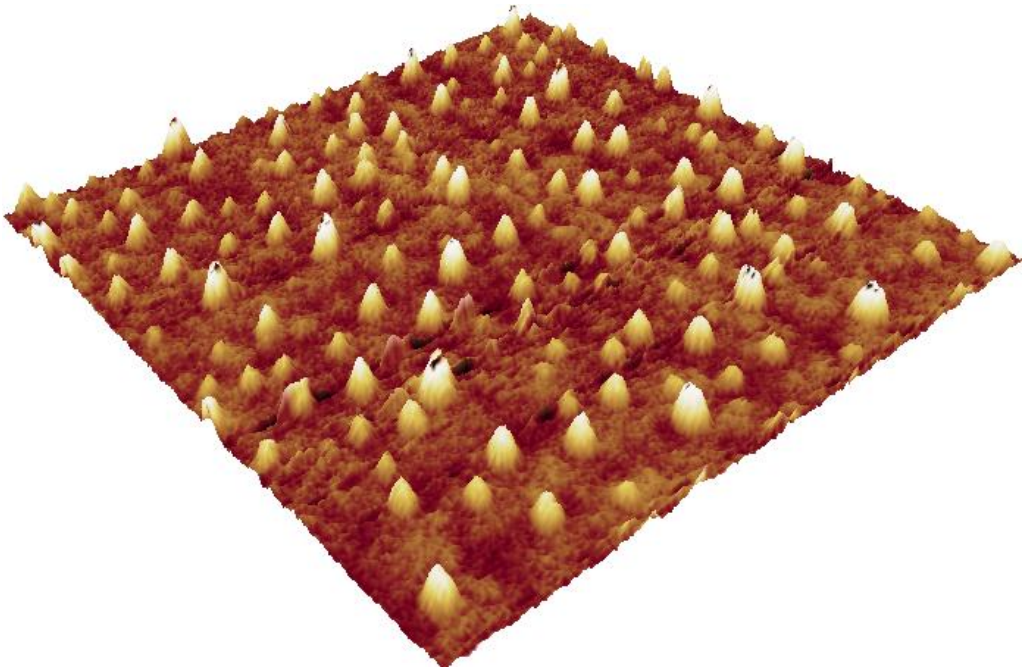

Figure 4. 5: AFM image of annealed ITO film

The grain size, thickness, roughness and height asymmetries values of ITO film estimated from the AFM images are depicted in Table 4.4. As seen from the table that the crystallite size value is observed to be about 64 nm. The average crystallite size deduced from the AFM measurements are generally greater than those inferred from the Scherrer method [110, 111]. However, all the data obtained are found to be good agreement with each other.

Statistical parameters	ITO film
Grain size from AFM (nm)	64
Average roughness (nm)	3.85
RMS roughness (nm)	3.96
Skewness, S_{sk}	1.10
Kurtosis, S_{ku}	1.31

Table 4. 4: Microstructural, morphological and statistical parameters of the annealed ITO film

Further, average roughness (S_a) and rms roughness parameter (S_q) are inferred from the AFM images. As reported in literature, the former is the arithmetic mean or average of the absolute distances of the surface points from the mean plane whereas the latter is the root mean square of the surface departures from the mean plane within the sampling area [106]. S_a value can be calculated by the relation 4.3 and S_q can be computed by the equation 4.4.

The S_a and S_q values obtained are given in Table 4.4. As seen from the table, the S_a of 3.85 and S_q of 3.96 are found to be the small values for the ITO film. Based on the results, the regular structures are observed on the surface of the film studied. However, the different surface roughness values might show the

possible reason for the variation of the oxygen vacancies in the ITO films prepared. Moreover, similar results were reported in the literature [100, 116].

The height asymmetries including surface skewness and kurtosis are determined from the height distribution histogram for the samples [107]. The surface skewness (S_{sk}) is a measurement for the symmetry of the variation of a surface about its mean plane whereas the surface kurtosis (S_{ku}) is a measurement of the peakedness or sharpness of a surface. The inner and latter of a sample can be computed from equation 4.5 and 4.6.

The S_{sk} and S_{ku} values calculated are listed in Table 4.4. One can see from the table that the surface skewness is obtained to be positive for all the samples while the surface kurtosis is found to be less than 3. According to the combination of the skewness and kurtosis values, the ITO film surface is found to be spread out distribution and comprised of disproportionate number of peaks [109]. In conclusion, the ITO thin film produced in this work can be useful for applications in technology and industry.

4.3 Transmittance Spectra

4.3.1 Transmittance Spectra of TiO_2

Homogeneity, porosity and refraction index of a film can be determined by transmittance spectra, such that high transmittance of the film indicates its low surface roughness, low refraction index, high porosity and good homogeneity [109,117]. Figure 4.6 depicts the transmittance spectra as a function of wavelength in the wavelength range 300–700 nm for TiO_2 thin film. It is apparent

from the figure that the amplitude of interference oscillation of the thin film is obtained to be 89%.

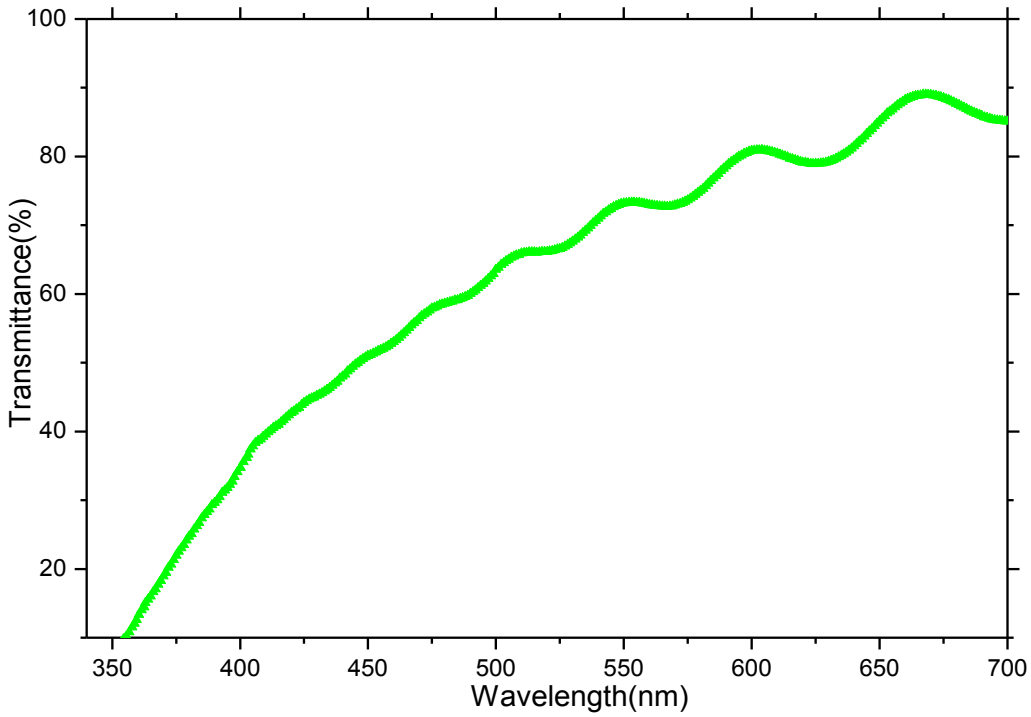

Figure 4. 6: Optical transmittance spectra of TiO_2 thin film deposited on Soda lime glass

4.3.2 Transmittance Spectra of ITO

It is argued that homogeneity, optical band gap energy, refraction index, porosity and photocatalytic performance of a film can be determined with the aid of transmittance spectra [109]. The higher transmittance a thin film exhibits the better homogeneity, smaller crystallite size, lower refraction index, higher porosity and greater energy band gap the film obtains [117]. Figure 4.7 shows the transmittance spectra as a function of wavelength in the wavelength range 300–700 nm for the ITO thin film prepared in this work. As seen from the figure the ITO film produced exhibits high optical transmittance 93% in the wavelength

range performed as result of the larger growth of particles, which are already supported by both XRD and AFM results. Based on these results, the ITO film has the large crystallite size and the fine optical property.

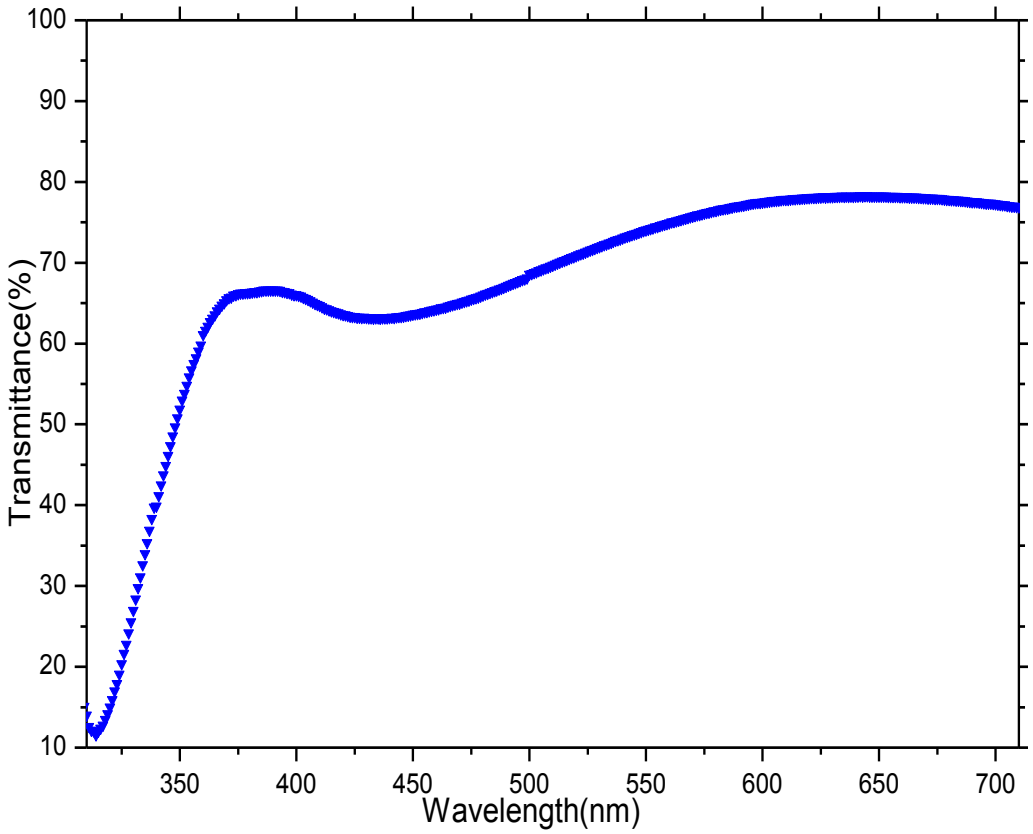

Figure 4. 7: Optical transmittance spectra of the ITO thin film

4.4 Refractive Index, Packing Density and Porosity Analyses

4.4.1 Refractive Index, Packing Density and Porosity Analyses of TiO_2

The refractive index, a fundamental property of a thin film, is closely associated with the electronic polarizability of ions and the local field inside the film [118]. The refractive index (n_λ) and porosity of the prepared TiO_2 film is tabulated in Table 4.5.

Parameters	TiO_2 film
Refraction index	2.08
Porosity (%)	56.12
Optical Band gap energy (eV)	3.2

Table 4. 5: Refraction index, porosity and optical band gap energy of TiO_2 film

The former is calculated from the optical transmittance data by means of the Swanepoel's envelope method [119], which is based on the analysis of the transmittance spectrum of a weakly absorbing film deposited on a non-absorbing substrate [120]. Hence, the refractive index (n_λ) over the spectral range is deduced from the envelopes fitted to the extrema measured:

$$n_\lambda = \left[N + (N^2 - n_0^2 n_1^2)^{1/2} \right]^{1/2} \quad 4.7$$

$$N = 2n_0 n_1 \left[(T_{M(\lambda)} - T_{m(\lambda)}) / T_{M(\lambda)} T_{m(\lambda)} \right] + (n_0^2 + n_1^2)/2 \quad 4.8$$

where $T_{M(\lambda)}$ and $T_{m(\lambda)}$ are the transmittance maximum and minimum of the film at a wavelength λ; n_0 denotes the refractive index of air, and n1 is the refractive index of the substrate, respectively. The TiO_2 film prepared is assumed as homogeneous structures in calculation. Table 4.5 indicates that the calculated refractive index of the TiO_2 film is observed to be 2.08. In the literature the index of the TiO_2 structure is reported in a range of 1.2–2.4. This wide change in the refractive

index stems from the variation of the oxygen in the TiO_2 film [121-123]. Moreover, the latter (porosity of the TiO_2 film) is calculated with the aid of the following equation [124]:

$$\text{Porosity} = (1 - \frac{n^2 - 1}{n_d^2 - 1}) \times 100(\%) \qquad 4.9$$

where the n_d is 2.52 (the refractive index of pore-free anatase) [40] when the n denotes the refractive index of the porous thin films. The porosity values calculated are also given in Table 4.5. It is visible from the table that the porosity is found to be about 56.1% for the TiO_2 film, favored by AFM images. The high porosity value allows to the more dye cover the structure of TiO_2 and so the cell obtained is more sensitive to illumination.

4.4.2 Refractive Index, Packing Density and Porosity Analyses of ITO

Table 4.6 indicates the refractive index and porosity (evaluated from n_λ) values of the ITO films prepared at 400 ^{0}C annealing temperature.

Electro-optical characteristics	ITO film
Refraction index	1.94
Porosity (%)	18.96
Packing density	1.487
Optical band gap energy (eV)	3.68

Table 4. 6: Electro-optical characteristics of the ITO film

The former is derived from the optical transmittance data with the aid of the Swanepoel's envelope method [119, 120]. The refractive index of the ITO film is inferred from the envelopes fitted to the extrema measured by the equation 4.7 and 4.8.

The refractive index of the ITO sample studied in this work is calculated to be 1.94. However, the refractive index calculated for the sample is smaller than the values reported in [125] and [126] as a result of lesser packing density of grains and lower oxygen vacancies in the sample studied, which means that the refractive index plays an important role on the determination of the packing density. In this study, the packing density of the ITO sample is deduced from the equation 4.9 [127,128],

$$n^2 = \frac{(1-p)n_v^4 + (1+p)n_v^2 n_s^2}{(1+p)n_v^2 + (1-p)n_s^2} \qquad 4.10$$

where n is the refractive index of the film studied, n_s denotes the substrate refractive index, $n_v$represents the void refractive index (n_v =1.00 for air) and p is the packing density. The packing density is obtained to be about 1.487 for the ITO sample, respectively.

Additionally, the porosity value of the ITO film is determined from the equation 4.9. The porosity value calculated is listed in Table 1. The porosity of ITO film is found to be about 37.8%. Based on the results, the ITO film has less porous compared to the TiO_2 thin film, attributed to the increase of the conductivity of the ITO film. Therefore, the efficiency and maximum power of the cell enhance automatically.

4.5 Optical Band Gap Energy Analysis

4.5.1 Optical Band Gap Energy Analysis of TiO_2

As well known, there are several models and reports to find the optical absorption coefficient (α) and optical band gap energy (E_g) of a material [129]. In this thesis, we assume an indirect transition (value of the energy separation between the top of the valence band and the bottom of the conduction band) for the determination of the optical band gap of the film by means of the following relation [130]:

$$\alpha(h\nu) \infty A(h\nu - E_g)^2 \qquad 4.11$$

where α denotes absorption coefficient when A presents the edge width parameter and $h\nu$ is the photon energy. Figure 4.8 illustrates $(\alpha h\nu)^2$ versus photon energy (eV) plots for the TiO_2 film respectively. The band gap value of the film is deduced from the extrapolation of the linear plots of $(\alpha h\nu)^{1/2}$ versus hν when (α = 0). The energy gap is found to be about 3.2 eV for the TiO_2.

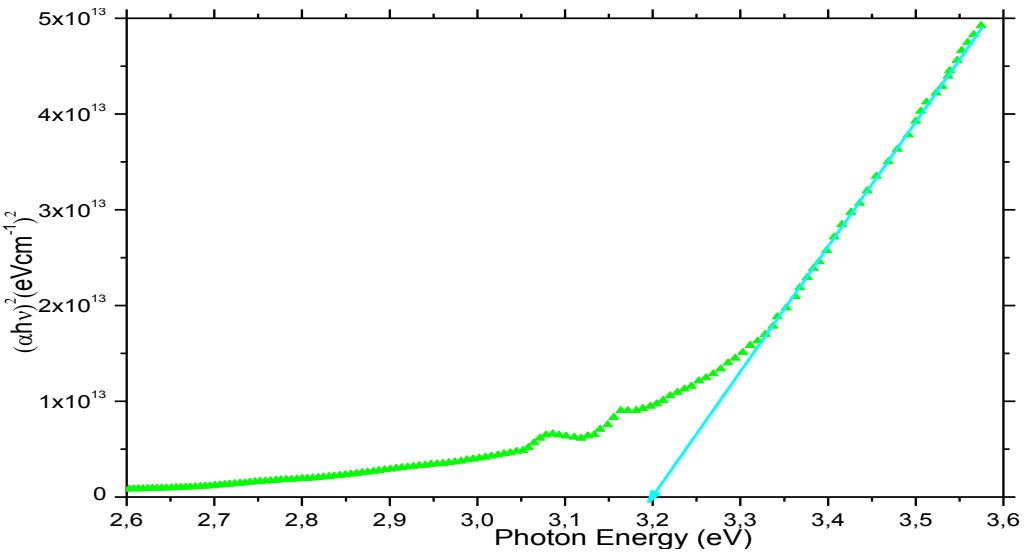

Figure 4. 8: Optical absorption coefficient α versus band gap energy (E_g) of TiO_2 thin film

4.5.2 Optical Band Gap Energy Analysis of ITO

Figure 4.9 illustrates $(\alpha h\upsilon)^2$ versus photon energy (eV) plots for the ITO thin film prepared. The energy band gap is deduced from the extrapolation of the linear plots of $(\alpha h\upsilon)^{1/2}$ versus $h\upsilon$ when ($\alpha = 0$). The estimated values of optical energy band gap are obtained to be 3.68 eV. According to these results, the energy band gap for the ITO film is obtained to shift to higher energy value due to the larger grain size and less porous structure compared to the TiO_2 film [131–135]. However, wide range of the band gap for the degenerate superconductor oxides (both the TiO_2 and ITO film) stems from two competing mechanisms: the first one is the band gap narrowing because of the electron-electron and electron-impurity effects on the valence and conduction bands, the second mechanism is the band gap widening by the Burstein-Moss effect due to the blocking of the lowest states of the conduction band by means of the excess electrons.

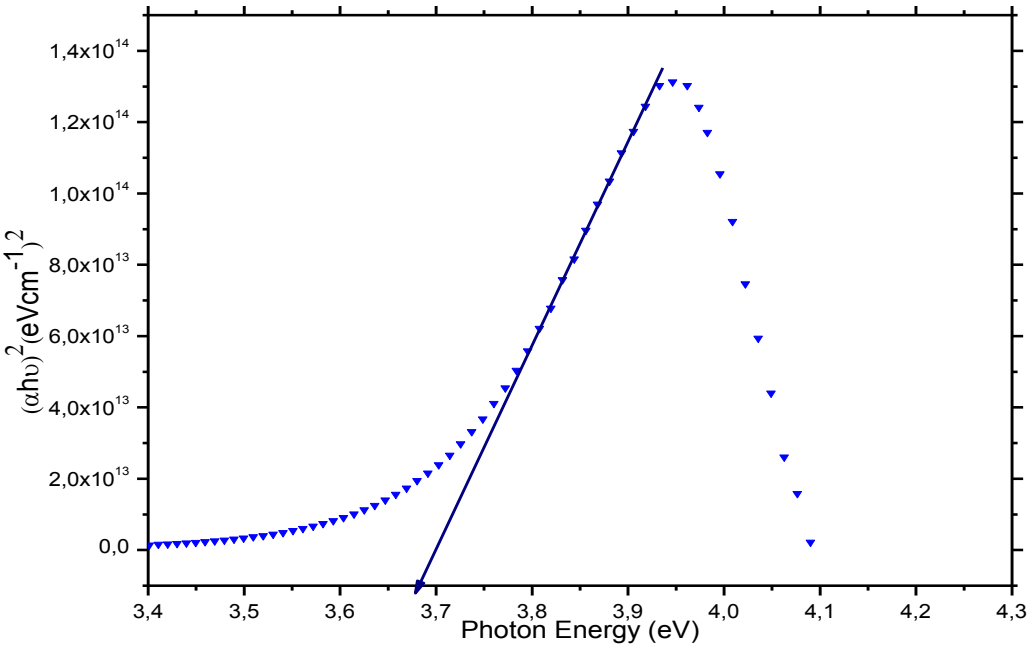

Figure 4. 9: Optical absorption coefficient α versus band gap energy (E_g) of the ITO film

4.6 SEM Characterization of TiO_2

The surface structure, orientations of the grains and accumulation in the grain boundaries of the TiO_2 thin film is conducted by means of Scanning Electron Microscopy (SEM) images taken in the secondary electron image mode. Fig. 4.10 indicates the SEM image of the fractured surface of the TiO_2. It is apparent from the figure that the TiO_2 film surface has a fine crystalline homogeneous structure consisting of the smooth and spherical nano-sized crystallites on the film surface. Moreover, uniform particle distribution is observed on the surface as a result of the regular grain size. Additionally, it is visible that form fig. 4.10, the TiO_2 film has porous structure, hence the dye covers the particle of TiO_2 better and it is more sensitive to light absorption, supported by the results of the transmittance spectra investigations.

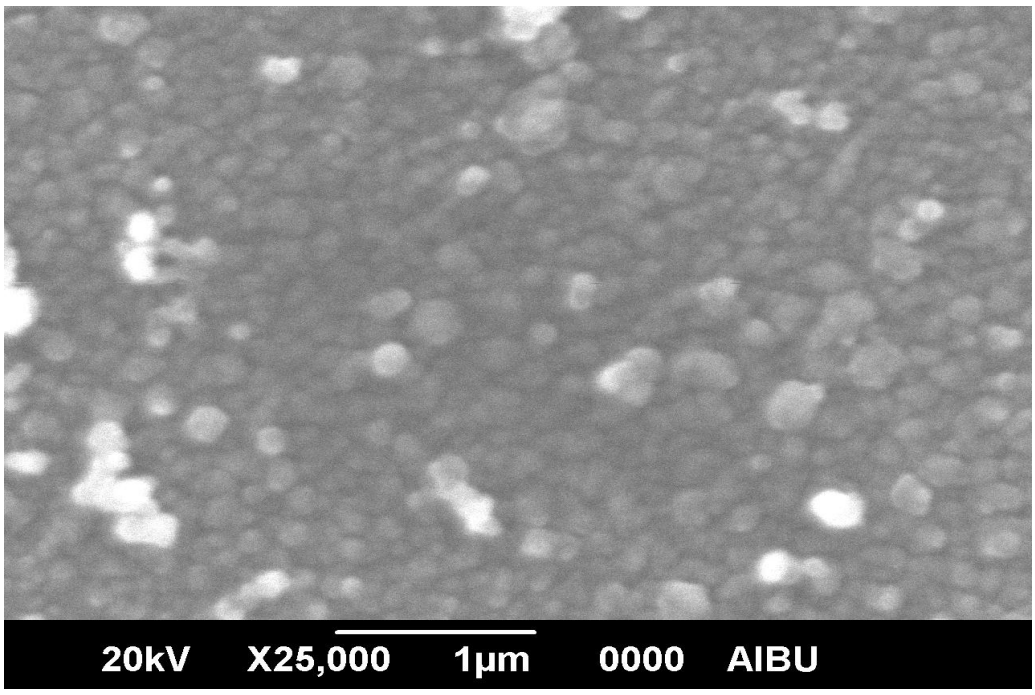

Figure 4. 10: SEM image of TiO_2

4.7 Current-voltage Characterization of the Cell

The efficiency of the cell was calculated from I-V curve displayed in fig. 4.11. Firstly, the Fill Factor (FF) was determined from the equation 4.12.

$$FF = \frac{P_{max}}{J_{SC}V_{OC}} = \frac{J_{max}V_{max}}{J_{SC}V_{OC}} \quad 4.12$$

where $J_{SC} = \frac{I_{SC}}{A}$ and $J_{max} = \frac{I_{max}}{A}$, A is the active area of the cell.

After calculation of the FF, the efficiency of the cell was computed with the aid of the equation 4.13.

$$\eta = \frac{P_{max}}{P_{input}} = \frac{V_{OC}J_{SC}FF}{P_{input}} \quad \text{for the efficiency.} \quad 4.13$$

where P_{input} = 1 kW/m^2 and active area, A = 4cm^2

Finally the maximum power was calculated by the equation 4.14.

$$P_{max} = V_{OC}I_{SC}\,FF \quad 4.14$$

The measured and calculated results are tabulated in Table 4.7.

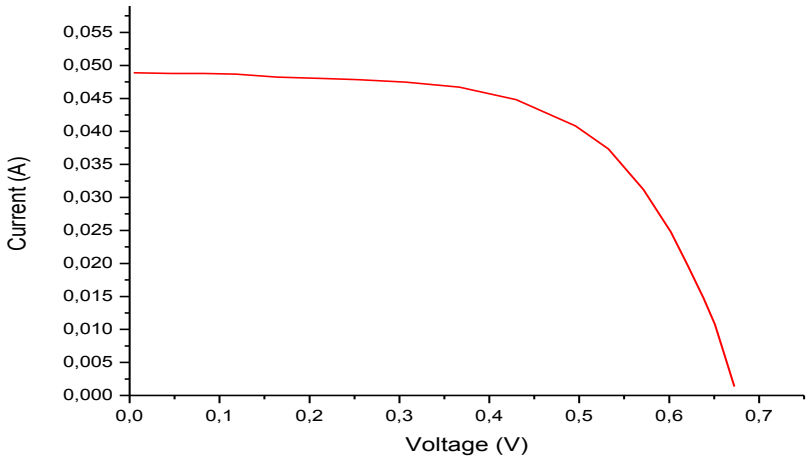

Figure 4. 11: Current-voltage graph of the DSSC

Efficiency (%)	FF (%)	I_{sc} (mA)	V_{oc} (V)	P_{max} (mW)
5,05	63,4	47	0,68	20,1

Table 4. 7: Results of I-V curve of the DSSC

As a result, an efficient dye sensitized solar cell was obtained by spray pyrolysis method of coating the nanocrystalline TiO_2. However, the measured efficiency of the DSSC can be influenced by heat in DSSC, surface parameter, photocurrent loss and absorption of incident light factor. Overall, the dye sensitized solar cell can be used as an energy source.

REFERENCES

[1] K. Butti and J.Perlin, p. 63, 77, 101 (1981).

[2] K. Butti and J.Perlin, p. 249 (1981).

[3] D. Yergin, p. 634, 653-673 (1991).

[4] J.N. Shive andV. Nostrand, Semiconductor Devices (1959).

[5] D. Anderson, Clean Electricity from Photovoltaics, eds. M.D. Archer and R.D. Hill London: Imperial College Press (2001).

[6] M. Wolf, \Historical development of solar cells", Proc. 25th Power Sources Sym-posium, 1972. In Solar Cells, ed. C.E. Backus IEEE Press (1976).

[7] T. Markvart, L. Castañer, Practical Handbook of Photovoltaics: Fundamentals and Applications. New York. Elsevier, p.81 – 87 (2003).

[8] V. Zeghbroeck, B. Principles of semiconductor devices
Available: http://ece-www. colorado.edu/~bart/book/book/title.htm (2004).

[9] M.K. Nazeeruddin, A. Kay, I. Rodicio, R. Humpbry-Baker, E. Miiller, P. Liska, N. Vlachopoulos andM. Grätzel,J. Am. Chem. Soc. 115, p.6382-6390 (1993).

[10] A. Hagfeldt and M. Grätzel, Chem. Rev. 95, p.49-68 (1995).

[11]C. J. Brabec, N. S. Sariciftci, and J. C. Hummelen, Plastic Solar Cells, Adv. Funct. Mater (2001).

[12] S.A. Haque, Y. Tachibana, D.R. Klug and J.R. Durrant, J. Phys. Chem. B., 102, p.1745-1749 (1998).

[13] S.A. Haque, Y. Tachibana, R.L. Willis, J.E. Moser, M. Grätzel, R. David, D.R. Klug, R. James and J.R. Durrant,J. Phys. Chem. B., 104, p.538-547 (2000).

[14] D. Cahen, G. Hodes, M. Grätzel, J.F. Guillemoles and I. Riess J. Phys. Chem. B., 104, p.2053-2059 (2000).

[15] B. O'Regan and M. Grätzel, Nature 353, p.737-740 (1991).

[16] S.Y. Huang, G. Schlichthörl, A.J. Nozik, M. Grätzel and A.J. Frank, J. Phys. Chem. B., 101, p.2576-2582 (1997).

[17] A. Hagfeldt, S. E. Lindquist and M. Grätzel, Solar Energy Materials and Solar Cells, 32, p.245 (1994).

[18] R. Kern, R. Sastrawan, J. Ferber, R. Stangl and J. Luther, Electrochimica Acta 47, p.4213-4225 (2002).

[19] Q. Wang, E. Moser-Jacques and M. Grätzel, J. Phys. Chem. B, 109, p.14945-14953 (2005).

[20] L.M. Peter, N.W. Duffy, R.L. Wang and K.G.U. Wijayantha, Journal of Electroanalytical Chemistry 524–525, p.127–136 (2002).

[21] A.C. Fischer, L.M. Peter, E.A. Ponomarev, A.B. Walker and K.G.U. Wijayantha, J. Phys. Chem. B., 104, p.949 958 (2000).

[22] L. Dloczik, O. Ileperuma, I. Lauermann, L.M. Peter, E.A. Ponomarev, G. Redmond, N.J. Shaw and I. Uhlendorf J. Phys. Chem. B., 101, p.10281-10289 (1997).

[23] O. Kohle, M. Grätzel, A.F. Meyer and T.B. Meyer, Advanced Materials 9(11), p.904 (1997).

[24] M. Grätzel, Comptes Rendus Chimie 9,578 (2006).

[25] L. Bay and K. West, Solar Energy Materials & Solar Cells 87, 613 (2005).

[26] (http://www.solaronix.com/technology/dyesolarcells/) (2005).

[27] A. Islam, H. Sugihara, H. Arakawa, J. Photchem. Photobiol. A, 158, 131 (2003).

[28] A. Kay, M. Graetzel, J. Phys. Chem. 97, 6272 (1993).

[29] S. Cherian, C. C. Wamser, J. Phys. Chem. B, 104, 3624 (2000).

[30] T. Komori andY. Amao J. Porpyrins Phthalocyanines 7, 131-136 (2003).

[31] K. Hara, M. Kurashige, Y. Dan-oh, C. Kasada, A. Shinpo, S. Suga, K. Sayama, H. Arakawa, New J. Chem. 27, 783-785, (2003).

[32] K. Hara, K. Sayama, Y. Ohga, A. Shinpo, S. Suga, H.Arakawa, Chem. Commun. 569-570, (2001).

[33] S. Ferrere, B. A. Gregg, New J.Chem. 26, 1155 (2002).

[34] A. Hagfeldt and M. Grätzel, Acc. Chem. Res. (2000).

[35] M. Zribi, M. Kanzari, B. Rezig, Thin Solid Films 516, 1476 (2008).

[36] K. Kato, A. Tsuzuki, H. Taoda, Y. Torii, T. Kato, and Y. Butsugan, J. Mater. Sci. 30, 837 (1995).

[37] A. I. Al-Homoudi, J. S. Thakur, R. Naik, G. W. Auner, and G. Newaz, Appl. Surf. Sci. 253, 8607 (2007).

[38] E. György, G. Socol, E. Axente, I. N. Mihailescu, C. Ducu, and S. Ciuca, Appl. Surf. Sci. 247, 429 (2005).

[39] E. György, E. Axente, I. N. Mihailescu, C. Ducu, and H. Du, Appl. Surf. Sci. 252, 4578 (2006).

[40] L. Miao, P. Jin, K. Kanekko, A. Terai, N. Nabatova–Gabain, and S. Tanemura, Appl. Surf. Sci. 212, 255 (2003).

[41] D. Yoo, Kim, S. Kim, C. H. Hahn, C. Lee, and S. Cho, Appl. Surf. Sci. 253, 3888 (2007).

[42] B. O. Regan, and M. Gratzel, Nature 353, 737 (1991).

[43] Y. Sato, H. Akizuki, T. Kamiyama, and Y. Shigesato, Thin Solid Films 516, 5758 (2008).

[44] S. Murugesan, P. Kuppusami, N. Parvathavarthini, and E. Mohandas, Surf. Coat. Technol. 201, 7713 (2007).

[45] J. Osterwalder, T. Droubay, T. Kaspar, J. Williams, C. M. Wang and S. A. Chambers, Thin Solid Films 484, 289 (2005).

[46] M. O. Abou–Helal, and W. T. Seeber, Appl. Surf. Sci. 195, 53 (2002).

[47] A. Brevet, F. Fabreguette, L. Imhoff, M. C. Marco de Lucas, O. Heintz, L. Saviot, M. Sacilotti, and S. Bourgeois, Surf. Coat. Technol. 151–152, 36 (2002).

[48] G. S. Hermann, Y. Gao, T. T. Tran, and J. Osterwalder, Surf. Sci. 447, 201 (2000).

[49] S. Sen, S. Mahanty, S. Roy, O. Heintz, S. Bourgeois, and D. Chaumont, Thin Solid Films 474, 245 (2005).

[50] B. Hunsche, M. Vergöhl, and A. Ritz, Thin Solid Films 502, 188 (2006).

[51] Y. L. Wang, and K. Y. Zhang, Surf. Coat. Technol. 140, 155 (2001).

[52] S. H. Oh, D. J. Kim, S. H. Hahn and E. J. Kim, Mater. Lett. 57, 4151 (2003).

[53] J. Pascual, J. Camassel and H. Mathieu, Phys. Rev. Lett. 39, 1490 (1977).

[54] S. Banerjee, J. G. Gopal, P. Muraleedharan, A. K. Tyagi, and B. Raj, Curr. Sci. 90, 1378 (2006).

[55] M. C. Ferrara, L. Pilloni, S. Mazzarelli, and L. Tapfer, J. Phys. D Appl. Phys. 43, 095301 (2010).

[56] Y. Zhang, X. Ma, P. Chen, and D. Yang, J. Cryst. Growth 300, 551 (2007).

[57] J. Musil, D. Herman, and J. Sicha, J. Vac. Sci. Technol. A 24, 521 (2006).

[58] D. Luca, D. Mardare, F. Iacomi, and C. M. Teodorescu, Appl. Surf. Sci. 252, 6122 (2006).

[59] D. Chen, F. Huang, Yi-B. Cheng, and R. A. Caruso, Adv. Mater. 21, 2206 (2009).

[60] J. Touskova, J. Kovanda, L. Dobiasova, V. Parizek, and P. Kielar, Sol. Energ. Mat. Sol. C. 37, 65 (1995).

[61] C. G. Hamberg, K. F. Granqvist, B.E. Berggren, Sernelius, and L. Engstrom, Vacuum 35, 9 (1985).

[62] A. Romeo, M. Terheggen, D. Abou-Ras, D.L. Batzner, F.J. Haung, M. Kalin, D. Rudman, and A. N. Tiwari, Prog. Photovolt: Res. Appl. 12, 93 (2004).

[63] H. M. Zeyada, M. M. El-Nahass, I.K. El-Zawawi, and E.M. El-Menyawy, Eur. Phys. J- Appl. Phys. 49, 10301 (2010).

[64] S. K. Poznyak, A. N. Golubev, and A. I. Kulak, Surf. Sci. 454, 396 (2000).

[65] D. G. Parker, and P. G. Say, Electron. Lett. 22, 7 (1986).

[66] M. C. de Andrade, and S. Moehlecke, Appl. Phys. A 58, 6 (1994).

[67] K. L. Chopra, P. D. Paulson, and V. Dutta, Prog. Photovolt: Res. Appl. 12, 69 (2004).

[68] R. Tueta, and M. Braguier, Thin Solid Films 80, 8 (1981).

[69] T. J. Coutts, X. Li, M. W. Wanlass, K. A. Emery, and T. A. Cessert, IEEE Electron. Device Lett. 26, 660 (1990).

[70] M. Masuda, K. Sakuma, E. Satoh, Y. Yamasaki, H. Miyasaka, and J. Takeuchi, in Proc. 6th Int. Electron. Manuf. Techn. Symp. 95 (1989).

[71] E. Takeda, T. Kawaguchi, Y. Nanno, H. Tsutsu, T. Tamura, S. Ishihara, and S. Nagata, Int. Display Res. Conf. 155 (Soc. Inf. Disp., CA, 1988).

[72] P. P. Deimel, B. B. Heimhofer, G. Krotz, H. J. Lilienhof, J. Wind, G. Muller and E. Voges, IEEE Photon. Technol. Lett. 2, 449 (1990).

[73] Y. S. Kim, Y. C. Park, S. G. Ansari, J. Y. Lee, B. S. Lee, and H. S. Shin, Surf. Coat. Technol. 173, 299 (2003).

[74] M. S. Hwang, H. J. Lee, H. S. Jeong, Y. W. Seo, and S. J. Kwon, Surf. Coat. Technol. 171, 29 (2002).

[75] S. H. Keshmiri, M. Rezaee-Roknabadi, and S. Ashok, Thin Solid Films 413, 167 (2002).

[76] S. Ishibashi, Y. Higuchi, Y. Ota, and K. Nakamura, J. Vac. Sci. Technol. A 8, 1403 (1990).

[77] I. Hamberg, and C. G. Grangvist, J. Appl. Phys. 60, R123 (1986).

[78] A. Antony, M. Nisha, R. Manoj, and M. K. Jayaraj, Appl. Surf. Sci. 225, 294 (2004).

[79] V. Senthilkumara, P. Vickramana, M. Jayachandran, and C. Sanjeevirajac, Vacuum 84, 864 (2010).

[80] H. Y. Yeom, N. Popovich, E. Chason, and D. C. Paine, Thin Solid Films 411, 17 (2002).

[81] H. Morikawa, and M. Fujita, Thin Solid Films 359, 61 (2000).

[82] M. J. Alam, and D. C. Cameron, Thin Solid Films 420–421, 76 (2002).

[83] Y. S. Jung, Solid State Commun. 129, 491 (2004).

[84] F. Zhu, C. H. A. Huan, K. Z. Hang, and A. T. S. Wee, Thin Solid Films 359, 244 (2000).

[85] Y. Nishio, T. Sei, and T. Tsuchiya, J. Mater. Sci. 31, 1761 (1996).

[86] H. S. Kwok, X. W. Sun, and D. H. Kim, Thin Solid Films 335, 299 (1998).

[87] H. Kim, A. Pique, and J. S. Horwitz, Appl. Phys. Lett. 74, 344 (1999).

[88] R. B. H. Tahar, T. Ban, Y. Ohya, and Y. Takahashi, J. Appl. Phys. 83, 2139 (1998).

[89] G. Yildirim, S. Bal, A. Varilci, J. Supercond. Nov. Magn. DOI 10.1007/s10948-012-1497-1 (2012).

[90] J. Economy, and R. Anderson, Inorg. Chem. 5, 989 (1966).

[91] G. Yildirim, A. Varilci, M. Akdogan, and C. Terzioglu, J. Mater. Sci: Mater. Electron. doi:10.1007/s10854-011-0522-7 (2011).

[92] B. D. Cullity, Element of XRD, 3rd Edition, (Addition-Wesley, ReadingMA, (2001).

[93] S. Bal, M. Dogruer, G. Yildirim, A. Varilci, C. Terzioglu, and Y. Zalaoglu, J. Supercond. Nov. Magn. doi: 10.1007/s10948-011-1360-9 (2011).

[94] J. H. Lee, J. Electroceram. 23, 554 (2009).

[95] C. W. Ow-Yang, D. Spinner, Y. Shigesato, and D. C. Paine, J. Appl. Phys. 83, 45 (1998).

[96] P. K. Song, H. Akao, M. Kamei, Y. Shigesato, and I. Y. Asui, Jpn. J. Appl. Phys. 38, 5224 (1999).

[97] N. Manavizadeh, A. Khodayari, E. Asl Soleimani, and S. Bagherzadeh, Iran. J. Chem. Chem. Eng. 28, 57 (2009).

[98] Y. Shigesato, and D. C. Paine, Thin Solid Films 238, 44 (1994).

[99] C. Guillen, and J. Herrero, Thin Solid Films 510, 260 (2006).

[100] L. Kerkach, A. Layadi, E. Dogheche, and D. Remiens, J. Phys. D: Appl. Phys. 39, 184 (2006).

[101] J. Ye, and K. Nakamura, Phys. Rev. B 48, 7554 (1993).

[102] S. Shin, Mater. Res. Bull. 16, 299 (1981).

[103] W. F. Wu, and B. S. Chiou, Thin Solid Films 293, 244 (1997).

[104] E. Fortunato, I. Ferreira, F. Giuliani, P. Wurmsdobler, and R. Martins, J. Non-Cryst. Solids 1213, 266 (2000).

[105] M. Gokcen, S. Bal, G. Yildirim, M. Gulen, and A. Varilci, J. Mater. Sci: Mater. Electron. DOI: 10.1007/s10854-012-0690-0 (2012).

[106] I. V. Tudose, P. Horvath, M. Suchea, S. Christoulakis, T. Kitsopoulos, and G. Kiriakidis, J. Appl. Phys. 89, 57 (2007).

[107] C. S. Yadav, and P. L. Paulose, New J. Phys. 11, 103046 (2009).

[108] G. Yildirim, S. Bal, M. Gulen, A. Varilci, E. Budak, and M. Akdogan, Cryst. Res. Technol. 47, 195 (2012).

[109] G. Yildirim, M. Akdogan, A. Varilci, and C. Terzioglu, Cryst. Res. Technol. 45, 1161 (2010).

[110] H. Kim, J. S. Horwitz, G. Kushto, A. Pique, Z. H. Kafafi, C. M. Gilmore, and D. B. Chrisey, J. Appl. Phys. 88, 6021 (2000).

[111] G. Korotcenkov, V. Brinzari, A. Cerneavschi, M. Ivanov, V. Golonvanov, A. Cornet, J. Morante, A. Cabot, and J. Arbiol, Thin Solid Films 406, 315 (2004).

[112] P. Thilakan, C. Minarini, S. Loreti, and E. Terzini, Thin Solid Films 388, 34 (2001).

[113] D. Kim, Y. Han, J. S. Cho, and S. K. Koh, Thin Solid Films 377/378, 81 (2000).

[114] G. Jayalakshmi, N. Gopalakrishnan, B. K. Panigrahi, and T. Balasubramanian, Crst. Res. Technol. 12, 1257 (2011).

[115] B. L. Zhu, X. Z. Zhao, S. Xu, F. H. Su, G. H. Li, X. G. Wu, J. Wu, R. Wu, and J. Liu, Jpn, J. Appl. Phys. 47, 2225 (2008).

[116] H. Kim, and C. M. Gilmore, J. Appl. Phys. 86, 6451 (1999).

[117] R. Thomas, D. C. Dube, M. N. Kamalasanan, and S. Chandra, Thin Solid Films 346, 212 (1999).

[118] M. M. El-Nahass, E. M. El-Menyawy, Mater. Sci. Eng. B-Adv. 177, 145 (2012).

[119] R. Swanepoel, J. Phys. E, Sci. Instrum. 16, 1214 (1983).

[120] J. C. Manifacier, J. Gasiot, and J. P. Fillard, J. Phys. E 9, 1002 (1976).

[121] J. K. Yao, Z. X. Fan, Y. X. Jin, Y. A. Zhao, H. B. He, and J. D. Shao, J. Appl. Phys. 102,063105 (2007).

[122] J. K. Yao, Z. X. Fan, Y. X. Jin, Y. A. Zhao, H. B. He, and J. D. Shao, Thin Solid Films 516, 1237 (2008).

[123] J. K. Yao, J. D. Shao, H. B. He, and Z. X. Fan, Appl. Surf. Sci. 253, 8911 (2007).

[124] B. E. Yoldas, and P. W. Partlow, Thin Solid Films 129, 1 (1985).

[125] W. W. Mobzen, J. Vac. Sci. Technol. 12, 99 (1975).

[126] J. Szczyrbowski, A. Dietrich and H. Hoffmann, Phys. Stat. Sol. A 78, 243 (1983).

[127] H. A. Macleod, J. Vac. Sci. Technol. A 4, 418 (1986).

[128] W. L. Bragg, and A. B. Pippard, Acta Crystallogr. 6, 865 (1953).

[129] H. N. Cui, V. Teixeira, and A. Monteiro, Vacuum 67, 589 (2002).

[130] J. I. Pankove, Optical Processes in Semiconductors, 2nd Edition (Dover Publications Inc., New York, 1970).

[131] Y. D. Glinka, S. H. Lin, L. P. Hwang, Y. T. Chen, and N. H. Tolk, Phys. Rev. B 64, 085421 (2001).

[132] G. L. Tian, H. B. He, and J. D. Shao, Chinese Phys. Lett. 22, 1787 (2005).

[133] F. M. Liu, T. M. Wang, J. Q. Li, C. Wang, S. K. Zheng, and M. Duan, J. Magn. Magn. Mater. 251, 245 (2002).

[134] Y. K. Chang, H. H. Hsieh, W. F. Pong, M. H. Tsai, F. Z. Chien, P. K. Tseng, L. C. Chen, T. Y. Wang, K. H. Chen, D. M. Bhusari, J. R. Yang, and S. T. Lin, Phys. Rev. Lett. 82, 5377 (1999).

[135] J. T. Jiu, F. M. Wang, and M. Adachi, Mater. Lett. 58, 3915 (2004).